remote sensing

MDPI

Article

Revealing Spatiotemporal Characteristics of Global Seismic Thermal Anomalies: Framework Based on Annual Energy Balance and Geospatial Constraints

Peng Yang [1], Guanlan Liu [1], Cheng Xing [1,*], Liang Zhong [2], Yaming Xu [1] and Jian Yu [1]

[1] School of Geodesy and Geomatics, Wuhan University, Wuhan 430079, China; yangpeng@whu.edu.cn (P.Y.); glliu@sgg.whu.edu.cn (G.L.); ymxu@whu.edu.cn (Y.X.); sword10@whu.edu.cn (J.Y.)
[2] School of Computer and Information Engineering, Xiamen University of Technology, Xiamen 361024, China; zliang@xmut.edu.cn
* Correspondence: chxing@sgg.whu.edu.cn

Highlights

What are the main findings?

- Developed a dynamic spatiotemporal adaptive framework that reveals the evolution of thermal anomalies from mixed to polarized states.
- Proposed the AEP to quantify spatiotemporal clustering, confirming its significant statistical linkage to seismic activity.

What are the implications of the main findings?

- Enables region-specific adaptive detection, advancing seismic thermal anomaly research toward spatiotemporal evolution.
- Identifies spatial heterogeneity as the key characteristic, linking anomaly persistence and co-seismic relevance, and focusing attention on AEP clustering regions.

Abstract

Thermal anomalies serve as potential earthquake precursors and are crucial for understanding the mechanisms underlying seismogenic mechanisms and geodynamic perturbations. To address the limited understanding of the polarity evolution of thermal anomalies, we developed a dynamic spatiotemporal adaptive framework to quantify global thermal anomaly responses. Four parameters—the coefficient of determination (R^2), spatiotemporal uncertainty (SU), temporal–spatial uncertainty ratio (TSUR), and spatiotemporal correlation coefficient (SCC)—were established to characterize the spatiotemporal patterns of thermal anomaly responses. Additionally, the Anomaly Emphasis Proximity (AEP) was introduced to identify statistically significant thermal anomaly events. The results indicate that the spatiotemporal evolution of thermal anomalies exhibits a transition from pre-earthquake mixed anomalies (both positive and negative) to post-earthquake unipolar anomalies (TIB decreased from 92% to 49%), accompanied by pronounced sea–land differentiation (SST increased from 0.3% to 98.7%). The AEP reveals significant thermal anomaly clustering highly consistent with earthquake activity (e.g., the 2008 Mw 8.0 Wenchuan earthquake in the Qinghai–Tibet Plateau), showing strong correlations in structurally active regions (e.g., SCA and SWS; FDR < 18.5%, STCW > 3.7%) but weaker ones in stable regions (e.g., CNA and ECA). Overall, this framework significantly enhances the robustness and reliability of seismic thermal anomaly detection.

Check for updates

Academic Editors: Gianluca Groppelli, Jie Zhao, Shufang Tian, Ying Zhang and Die Hu

Received: 23 October 2025
Revised: 4 January 2026
Accepted: 12 January 2026
Published: 15 January 2026

Copyright: © 2026 by the authors. Licensee MDPI, Basel, Switzerland. This article is an open access article distributed under the terms and conditions of the Creative Commons Attribution (CC BY) license.

Keywords: pre-earthquake; thermal anomalies; earthquake precursors; spatiotemporal uncertainty; anomaly emphasis proximity (AEP); energy balance

1. Introduction

Given the increasing coupling between global population density and urbanization, investigating potential precursory signals of earthquakes is vital for reducing disaster impact—particularly in tectonically active subduction zones such as the circum-Pacific seismic belt [1,2]. A growing body of literature has reported a variety of geophysical and atmospheric anomalies preceding seismic events [3–7]. With the advancement of computing and remote sensing technologies, it is now feasible to monitor large areas with high temporal and spatial resolution [8]. Specifically, long-term thermal infrared datasets over seismically active regions enable the characterization of surface thermal anomalies prior to earthquakes, suggesting their potential as early warning indicators [9–12]. However, significant challenges remain. The spatial and temporal heterogeneity of thermal anomalies, regional differences in signal-to-noise ratio, and the presence of confounding environmental factors continue to obscure the underlying mechanisms and limit the reliability of these anomalies as robust precursors [13].

In numerous ground and satellite observations, thermal anomalies are often identified as short-lived and spatially localized temperature variations that occur near earthquake epicenters before seismic events [14,15]. These anomalies typically appear from several months to a few days prior to an earthquake, depending on the temporal and spatial characteristics of the seismogenic process [16]. Their spatial coverage generally ranges from tens to several hundred thousand square kilometers [17–19], with temperature ranging from several to over ten kelvins [20–22], and durations of a few days to several weeks [23–29]. Collectively, these characteristic parameters constitute the fundamental spatiotemporal constraints for identifying seismic thermal anomalies.

However, characterizing anomalies based solely on the absolute magnitude of temperature differences may be an oversimplification. Although most reported pre-earthquake thermal anomalies in inland areas are positive [30,31], studies such as that by Zhong et al. have demonstrated that both positive and negative anomalies can occur [32]. This indicates that surface temperature changes before earthquakes are not restricted to warming trends but may also manifest as cooling signals, reflecting the combined influence of multiple environmental and tectonic factors. Due to differences in thermal regimes between land and ocean, the manifestation of temperature anomalies also varies [33,34]. For example, thermal signals may be amplified over snow-covered regions. Ouzounov and Freund observed negative sea surface temperature anomalies before certain offshore earthquakes [35], which they attributed to upwelling of cold bottom water caused by tectonic activity. In some coastal regions, both positive and negative anomalies have been documented under different tectonic settings, but the underlying mechanisms remain uncertain [36]. Therefore, limiting detection strictly to positive anomalies in earthquake-prone regions is insufficient.

Achieving reliable anomaly detection demands an integrated strategy combining theoretical constraints, observations, and physical validation [37]. To address this, various methods have been developed to detect pre-earthquake thermal anomalies, including the LST difference threshold [38], Z-score method [39,40], the Robust Satellite Techniques (RST) approach [41–43], temporal integration techniques [44], and other techniques [45–50]. While these approaches have demonstrated promising performance in selected case studies or localized regions, their limitations are also evident. On one hand, some methods do not sufficiently incorporate constraints from geophysical principles, resulting in a lack of

theoretical robustness when applied to complex natural processes [13,39]. On the other hand, external disturbances such as meteorological variability and anthropogenic influences may introduce systematic biases that compromise the stability and general applicability of these algorithms [51].

Since Gornyi et al. first proposed in 1988 that thermal infrared signals could serve as indicators of seismic activity [52], the field has undergone more than three decades of development. Although a large body of satellite-based thermal infrared observations has demonstrated a spatiotemporal correlation between thermal anomalies and earthquakes [53–55], the long-term statistical characteristics of such anomalies remain insufficiently understood [56–60]. Therefore, any investigation of potential pre-earthquake thermal anomalies must be grounded in robust geophysical theory and supported by systematic statistical analysis [61–63], rather than relying on arbitrary assumptions or speculative forecasts [20,64–66].

Although considerable progress has been made in the study of earthquake precursors [39,67,68], current findings remain insufficient for direct application to earthquake prediction, and the feasibility of related methods has yet to be fully validated [69]. Moreover, against the backdrop of global warming and the increasing frequency of extreme weather events, the influence of various meteorological factors on surface temperature further complicates the identification of pre-earthquake thermal anomalies [70–73]. Previous efforts to enhance forecasting capability by integrating multiple geophysical parameters have been hindered by substantial noise and regional variability in the data. This has led to inconsistent statistical results [33] and limiting the development of a unified and reliable early warning model [10,14]. These findings highlight that research on only a small number of earthquake events may not reveal spatiotemporal patterns.

In summary, the current understanding of the spatiotemporal variation in positive and negative thermal anomaly polarity remains limited. Furthermore, existing statistical characteristics exhibit instability, while radiative properties differ significantly between land and ocean surfaces. Recognizing that thermal anomalies may represent the lithosphere's initial response to external perturbations [74], this research develops a dynamic spatiotemporal adaptive framework to quantify response patterns in global earthquake-prone regions. To achieve this objective, two key scientific questions are addressed: (1) How can the spatiotemporal characteristics and evolutionary patterns of thermal anomalies be dynamically represented? (2) How are clusters of thermal anomalies spatiotemporally correlated with seismic activity?

To minimize the influence of climatic factors in global-scale statistical analyses, the temperature field was stratified using the IPCC AR6 climate zoning framework [75,76]. Meanwhile, we established specific features to characterize the spatiotemporal response of thermal anomalies. Based on the detection results, the evolutionary patterns of thermal anomalies were further analyzed, and an Anomaly Emphasis Proximity (AEP) index was introduced to identify statistically significant events. By analyzing 220,182 earthquakes of Mw $\geq$ 4 worldwide, the study evaluates the spatiotemporal statistical patterns of thermal anomalies [77], elucidates the mechanisms underlying enhanced detection capability, and provides new insights into the investigation of seismic thermal anomalies.

To ensure that the association between detected thermal anomalies and earthquakes is non-random, we systematically analyzed the spatiotemporal cube of the study area to obtain thermal anomalies for the full raster grid. These data are then used to test the statistical significance of the correlation between the detected anomalies and seismic events (Figure S9 in Supplementary File S3).

2. Materials and Methods

We integrated multiple open-access datasets from well-established global sources: (a) the global earthquake catalog provided by the United States Geological Survey (USGS), covering all events of $mag \geq 4$ since 2000; (b) daily near-surface land temperature data at 1 km resolution from 2003 to 2020, released by Iowa State University [78]; and (c) global daily sea surface temperature (SST) data at 5 km resolution from 2003 to 2020, obtained from NOAA CoastWatch's CoralTemp SST version 3.1 archive [79] (totaling 6575 daily records).

While statistical methods (e.g., RST, Z-Score) suppress noise effectively, they lack the physical basis to interpret seismic thermal mechanisms. Therefore, we introduce a hybrid framework coupling physical diffusion models with data-driven diagnostics. Employing the heat-diffusion equation on an ellipsoidal Earth as a baseline, we decompose observational residuals into temporal, spatial, and correlation uncertainties. This method integrates heat conduction constraints to enable the physically interpretable detection of seismic thermal perturbations (proof provided in Supplementary File S1).

2.1. Construction of Thermal Anomaly Response Parameters

We integrate physical diffusion models with statistical analysis to establish critical thresholds for arbitrary transient heat sources, thereby facilitating the detection of thermal anomalies potentially associated with seismic activity. In this context, we define a "thermal anomaly" as an event in which surface thermodynamic parameters within a specific geographic region exceed the confidence bounds of their intrinsic spatiotemporal variability.

Under ideal conditions, assuming Fourier's Law and local energy conservation apply within a finite neighborhood, the idealized heat diffusion equation is derived as follows:

$$\frac{\partial u(\boldsymbol{r},t)}{\partial t} = \alpha \nabla^2 u(\boldsymbol{r},t) \tag{1}$$

Conversely, in non-ideal scenarios, such as the presence of transient heat sources or energy imbalance, the heat equation evolves to:

$$\frac{\partial u(\boldsymbol{r},t)}{\partial t} = \alpha \nabla^2 u(\boldsymbol{r},t) + \frac{Q(\boldsymbol{r},t)}{\rho c} \tag{2}$$

Here, the temperature field is denoted by $u(\boldsymbol{r},t)$, thermal diffusivity by $\alpha = \frac{k}{\rho c}$, and the volumetric heat source (power density) by $Q(\boldsymbol{r},t)$. The symbols ρ, c, and k represent density, specific heat capacity, and thermal conductivity, respectively.

In practical contexts, although the exact nature and spatiotemporal behavior of the transient heat source $Q(\boldsymbol{r},t)$ may remain unknown, our focus lies in detecting abnormal thermal signals that deviate from the predictions of the ideal diffusion model. To this end, we define a diagnostic residual term that captures such deviations.

Let: $X = \frac{\partial u}{\partial t}, Y = \alpha \nabla^2 u, \Delta(\boldsymbol{r},t) = \frac{Q(\boldsymbol{r},t)}{\rho c}, \mathrm{Z}(\boldsymbol{r},t) = u(\boldsymbol{r},t), \hat{\mathrm{Z}}(\boldsymbol{r},t) = \mu_{clim}(\boldsymbol{r},t)$, which leads to the identity: $\Delta(\boldsymbol{r},t) = u(\boldsymbol{r},t) - \mu_{clim}(\boldsymbol{r},t) = X - Y$.

Here, $\mathrm{Z}(\boldsymbol{r},t)$ is the observed value $u(\boldsymbol{r},t)$ of the temperature field, $\hat{\mathrm{Z}}(\boldsymbol{r},t)$ is the background value μ_{clim} of the temperature field.

Thus, monitoring Δ is mathematically equivalent to estimating the normalized heat-source strength. If $\Delta(\boldsymbol{r}, t) \approx 0$: the system follows ideal diffusion equilibrium. If $\Delta(\boldsymbol{r}, t)$ shows significant departures from zero: an external heat source must be present.

However, in actual observations, the measured temperature field is influenced by various factors from the transmission path, causing fluctuations in $\Delta(\boldsymbol{r}, t)$. Thus, we establish the null hypothesis:

H_0: $Q(\boldsymbol{r}, t) = 0$, there is no external heat source.

Under the null condition, the diagnostic residual follows a zero-mean Gaussian distribution: $\Delta_{null} \sim \mathcal{N}(0, \sigma_\Delta^2)$.

This provides the theoretical foundation for the 3σ detection rule: values outside $[-3\sigma_\Delta, +3\sigma_\Delta]$ can be rejected with 99.7% confidence.

According to the definition of residuals, the uncertainty of residuals is determined by the joint distribution of the "time variation term" and the "spatial diffusion term". To describe the spatiotemporal characteristics of diagnostic residual term $\Delta(\mathbf{r}, t)$, we define the following three core indicators to describe spatiotemporal uncertainty (σ_Δ) in the spatiotemporal domain. The parameters, respectively, represent, temporal uncertainty (σ_X), spatial uncertainty (σ_Y), and their correlation coefficient (ρ_{XY}).

Temporal Uncertainty: Reflects the background fluctuation of the temporal derivative. Spatial Uncertainty: Captures the background variability of spatial diffusion. Correlation Coefficient: Describes the linear dependence between temporal and spatial contributions. Spatiotemporal Uncertainty (Final Threshold): This variance represents the theoretical fluctuation range of $\Delta(\boldsymbol{r}, t)$ in non-anomalous background conditions.

Applying the law of error propagation, the variance of the residual term $\Delta(\boldsymbol{r}, t)$ is given by:

$$\mathrm{Var}(\Delta) = \mathrm{Var}(X) + \mathrm{Var}(Y) - 2 \cdot Cov(X, Y) \tag{3}$$

Based on the residual formulation above, the combined spatiotemporal uncertainty can be expressed as:

$$\begin{cases} \sigma_\Delta = \sqrt{\sigma_X^2 + \sigma_Y^2 - 2\rho_{XY}\sigma_X\sigma_Y} \\ \sigma_X(s_0, t) = std\left(\dfrac{\partial u}{\partial t}\right) = \sqrt{\dfrac{1}{N-1}\sum_{i=1}^{N}\left(u(s_0, i) - \hat{u}(s_0, i)\right)^2} \\ \sigma_Y(s, t_0) = std\left(\alpha\nabla^2 u\right) = \sqrt{\dfrac{1}{M-1}\sum_{j=1}^{M}\left(u(j, t_0) - \hat{u}(j, t_0)\right)^2} \\ \rho_{XY} = Corr\left(\dfrac{\partial u}{\partial t}, \alpha\nabla^2 u\right) = \dfrac{\sum_m (u_t - \hat{u}_t)(u_s - \hat{u}_s)}{\sqrt{\sum_m (u_t - \hat{u}_t)^2 \sum_m (u_s - \hat{u}_s)^2}} \end{cases} \tag{4}$$

To determine the detection threshold σ_Δ, we adopt a data-driven approach. This method comprehensively evaluates the volatility and interrelationships of time and space terms by analyzing observation data within a certain spatiotemporal domain, to estimate the theoretical value σ_∞ in Formula (S47) (Supplementary File S1). Spatiotemporal Uncertainty (Final Threshold) represents the theoretical fluctuation range of Δ in non-anomalous background conditions.

Based on the quantified spatiotemporal uncertainty, a critical threshold for transient heat sources is established to identify anomalous thermal states within the target region. Within a continuous spatiotemporal domain, three times the spatiotemporal uncertainty

(including positive and negative) is defined as the critical threshold distinguishing external heat sources. The difference between observed values and the theoretical background is used as the thermal signal anomaly detection sequence. When this difference exceeds the upper critical threshold, a positive thermal anomaly is recorded ($Z - \hat{Z} > 3\sigma_\Delta$); when it falls below the lower critical threshold, a negative thermal anomaly is recorded ($Z - \hat{Z} < -3\sigma_\Delta$); values within the thresholds are considered normal ($-3\sigma_\Delta \leq Z - \hat{Z} \leq 3\sigma_\Delta$).

The complete anomaly-detection algorithm consists of:

1. Parameter estimation: Use background or historical data to compute σ_X, σ_Y, and ρ_{XY}, then derive the threshold σ_Δ.
2. Residual computation: Evaluate $\Delta(\boldsymbol{r}, t)$ from real-time observations.
3. Anomaly classification using the 3σ rule: $|\Delta(\boldsymbol{r}, t)| > 3\sigma_\Delta$

If the inequality holds, it is judged as an abnormal heat source event; otherwise, it is judged as background fluctuation (normal).

In practical observations, the background can only be estimated using long-term time series data. Given that non-ideal diffusion models exhibit only a relatively stable dynamic equilibrium, it is critical to examine whether the latest observations trend towards the background level. This behavior significantly influences the residual decomposition of the observed temperature field (Equation (S15) in Supplementary File S1).

Therefore, in the residual calculation step, it is necessary to calculate the Coefficient of Determination between the observed values and the background values. The higher the R^2, the more reliable the background estimation model.

The anomaly detection workflow involves four parameters related to spatiotemporal uncertainty and one to residual calculation.

$$\begin{cases} R^2 = 1 - \left(\sigma_X(t)/\sigma_{X,\mathrm{tot}}(t)\right)^2, \mathrm{R-squared}\ (R^2) \\ \sigma_\Delta = \sqrt{\sigma_X^2 + \sigma_Y^2 - 2\rho_{XY}\sigma_X\sigma_Y}, \mathrm{Spatiotemporal\ uncertainty\ (SU)} \\ \sigma_X/\sigma_Y = std\left(\frac{\partial u}{\partial t}\right)/std\left(\alpha\nabla^2 u\right), \mathrm{Temporal-spatial\ uncertainty\ ratio\ (TSUR)} \\ \rho_{XY} = Corr\left(\frac{\partial u}{\partial t}, \alpha\nabla^2 u\right), \mathrm{Spatiotemporal\ correlation\ coefficient\ (SCC)} \end{cases} \tag{5}$$

We define four metrics (R^2, SU, TSUR, SCC) that, beyond their mathematical interdependence, characterize orthogonal physical dimensions of the detection process. The Determination Coefficient (R^2) serves as a quality index for model fidelity, validating the background reconstruction against climatic trends. Spatiotemporal Uncertainty (SU) defines the dynamic detection threshold, quantifying the aggregate confidence interval for temperature deviations. The Temporal-Spatial Uncertainty Ratio (TSUR) identifies the dominant variance source; values exceeding unity distinguish rapid temporal transients (e.g., heating) from static spatial heterogeneity. Finally, the Spatiotemporal Correlation Coefficient (SCC) validates local structural coherence. Collectively, these metrics form a hierarchical system—validating background (R^2), defining magnitude (SU), and characterizing pattern (TSUR, SCC)—to ensure robustness in non-stationary environments.

2.2. Annual Energy Balance and Geospatial Constraints Detection Framework

Given that the estimation of spatiotemporal uncertainty and background residuals relies on data-driven procedures, the global domain lacks a standardized estimation work-

flow. We propose a detection framework that integrates annual-cycle energy balance constraints with geospatial priors. Incorporating physical constraints improves the reliability of thermal anomaly identification [80,81].

Geospatial constraint. Although previous studies have shown that the impact of earthquakes on surface temperature tends to propagate along fault zones, it is not feasible to comprehensively account for the geometry of every fault system, particularly in regions where no earthquake has yet occurred. To address this limitation, we assume that surface temperature disturbances induced by an earthquake are radially distributed around the epicenter within a defined radius. Given that most surface temperature datasets are provided in regular latitude–longitude grids, we apply a spherical geodesic distance constraint to extract relevant temperature data within the prescribed neighborhood.

Energy balance constraint. We assume that the net surface energy budget at any given location varies periodically due to Earth's revolution around the Sun, and remains approximately balanced over a full orbital cycle. According to the Stefan–Boltzmann law, the total energy exchange over one orbital period can be expressed as:

$$E = \int_0^C \varepsilon_i \cdot \sigma \cdot T_i^4 \, dt = \int_{t_0}^{t_0+C} \varepsilon_i \cdot \sigma \cdot T_i^4 \, dt = \text{constant} \tag{6}$$

In practice, by taking the orbital cycle $C = 365$ days, the above expression can be discretized as:

$$\sum_{i=1}^{365} \varepsilon_i \cdot T_i^4 = \sum_{j=1+\Delta t}^{365+\Delta t} \varepsilon_j \cdot T_j^4 \tag{7}$$

When the condition is satisfied, the total energy over a full cycle remains conserved.

$$T_i = \left(\frac{\varepsilon_i}{\varepsilon_{i+365}} \right)^{0.25} \cdot T_{i+365} \tag{8}$$

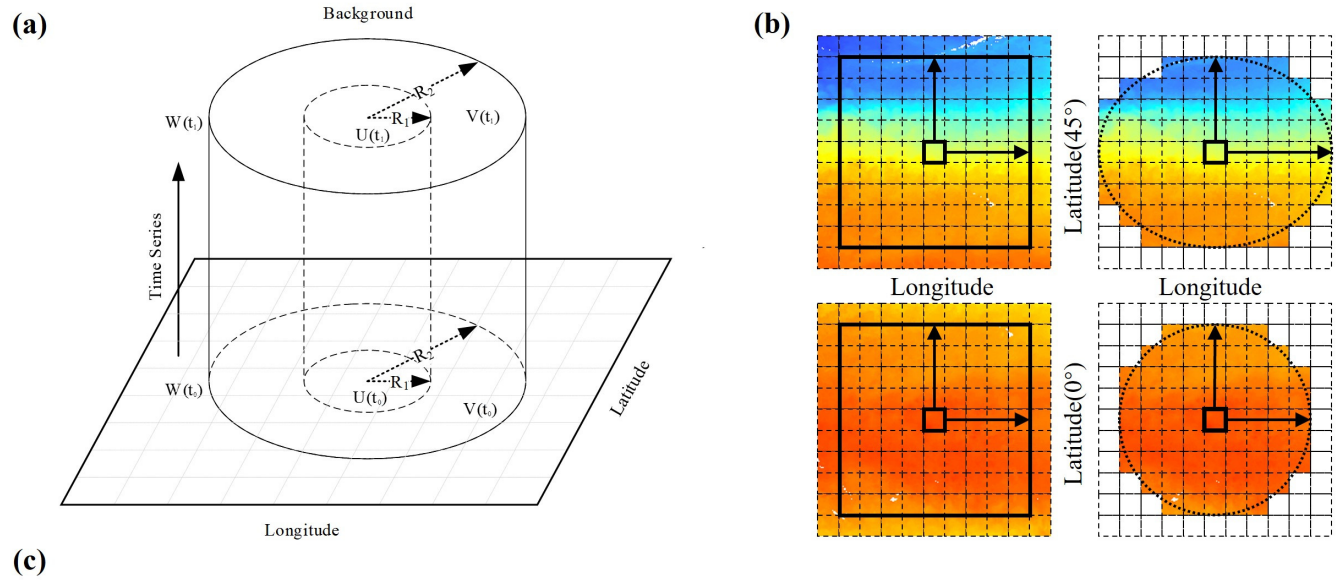
It should be noted that this equivalence relies on the assumption that interannual variations in surface emissivity and land cover are minimal, ensuring the validity of the energy balance constraint over climatological timescales.

However, actual multi-periodic constraints may be influenced by multiple factors, making it more difficult to recover the temperature change pattern. The formula for multi-periodic constraints is as follows:

$$\begin{cases} \mathrm{T}_i = \sum\limits_{k=1}^{m} \dfrac{A_k}{\omega_k} \sin(\omega_k t_i + \varphi_k) + B \\ \mathrm{E} = \int_{t_0}^{t_0+C} \varepsilon_i \cdot \sigma \cdot T_i^4 \, dt + B * C = \text{constant}, \quad i \in \mathbb{N}^+ \\ \omega_k = \dfrac{2\pi k}{C}, \quad k \in \mathbb{N}^+ \cup 1/\mathbb{N}^+, \end{cases} \tag{9}$$

where ω_k is a phase with a period of any number of days, A_k is the amplitude corresponding to phase ω_k; φ_k is its corresponding initial phase, t_i is the time, T_i is the daily temperature, B is the global average temperature, ε_i is the daily surface emissivity, C is the global period, and E is the total energy of the global period.

In practical detection, it is essential to define standardized input data. For a given earthquake event P_0 (characterized by occurrence time, magnitude, longitude, and latitude), the initial step is to select the time series within a spatial neighborhood defined by a specific geographic radius (Figure 1a). Due to grid projection effects, the number of grid points included within this radius varies with latitudes (Figure 1b).



(c)

Time series	Time series of surface temperature							
	First	…	Background	Before	Seismic	After	…	End
Attributes	Low correlation		2 year(730 days)	90 days	1 day	30 days	Low correlation	
			Obtain at the earthquake locations					

Figure 1. The spatiotemporal parameterization scheme based on annual energy balance and geographic constraints. (**a**) Schematic illustration of the spatiotemporal cube; (**b**) Conceptual diagram of neighborhood heterogeneity across different latitudes on the longitude–latitude grid; (**c**) Detailed parameter design of the spatiotemporal cube.

To facilitate robust baseline estimation, the dataset for each event is partitioned into a background set and a detection set. The detection set spans the interval from 90 days preceding the event to 30 days thereafter, while the background set comprises the two years immediately prior to the detection window (Figure 1c).

The detection procedure begins by inputting the event P_0 occurrence time to define the temporal range of the time series. The event's geographic coordinates (longitude and latitude) are then used to calculate the spatial neighborhood masks $U(P_0)$, $V(P_0)$, and $W(P_0)$ based on spherical distance constraints.

Subsequently, temperature raster data within the corresponding temporal window are extracted according to these masks. The spatiotemporal correlation coefficient is estimated using $U(P_0)$ and $V(P_0)$, while temporal and spatial uncertainties as well as observational biases are assessed with $W(P_0)$. Anomaly detection is then performed via a discriminant function. The entire detection workflow is iterated over all target earthquakes (Figure 2).

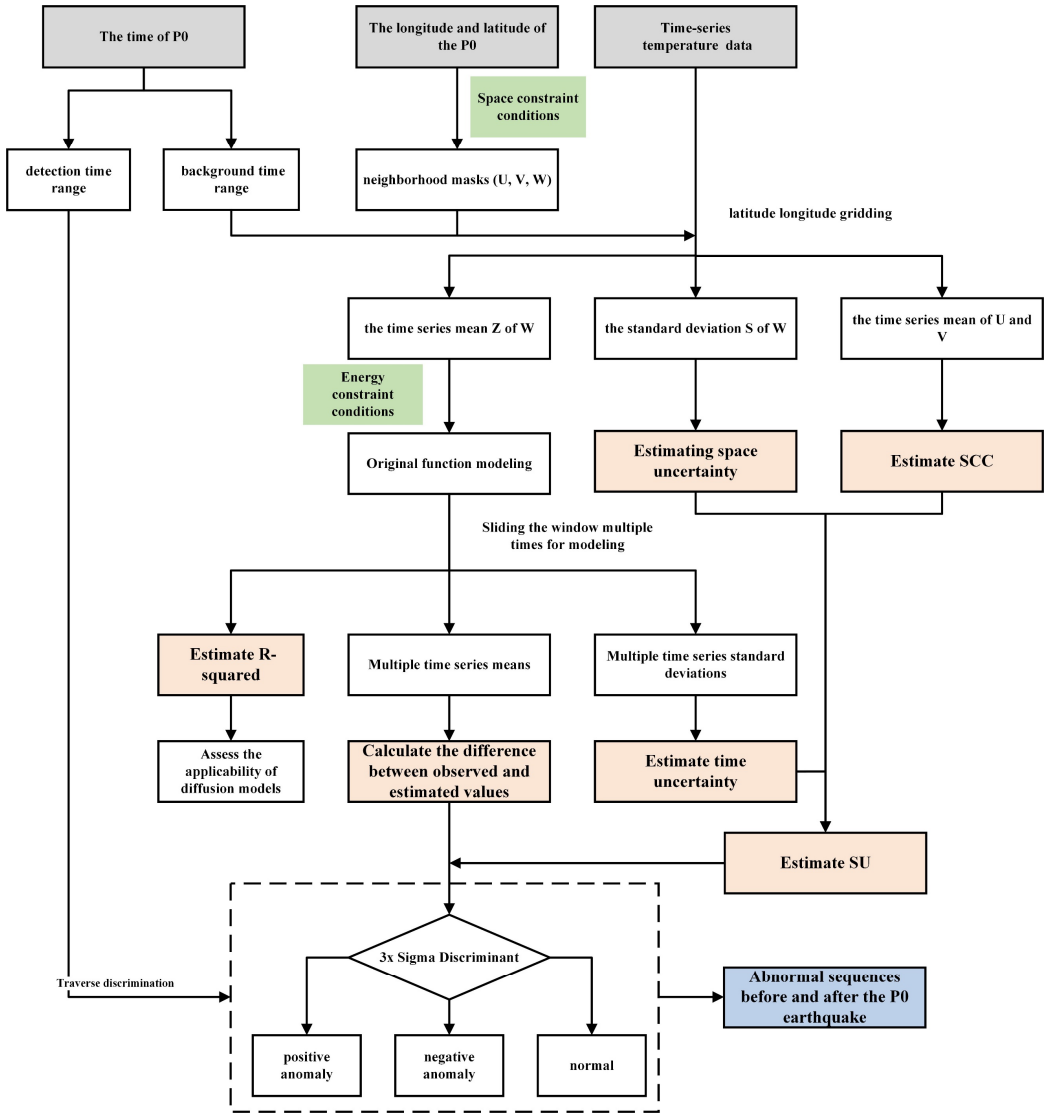


Figure 2. Detection algorithm flowchart.

2.3. Anomaly Emphasis Proximity Score (AEP)

Based on the globally detected time series of seismic thermal anomalies, to express the continuity and imminent nature of seismic thermal anomalies, we introduce the Anomaly Emphasis Proximity Score (AEP), a scalar metric computed from thermal anomaly detections within the 90 days preceding and 30 days following each earthquake. The AEP quantifies the joint significance of anomaly persistence and temporal proximity to the seismic event, thereby emphasizing continuous anomalies near the earthquake occurrence (Day 91). Given a binary time series of thermal anomalies during the pre-earthquake period, the AEP is defined as follows:

$$\mathbf{X} = \{x_1, x_2, \ldots, x_{90}\}, \quad x_t \in \{0, 1\} \tag{10}$$

where $x_t = 1$ denotes the presence of an anomaly on day t, we identify all consecutive anomaly segments as:

$$C = \{(t_1, l_1), (t_2, l_2), \ldots, (t_k, l_k)\} \tag{11}$$

with t_i being the start day of the ith anomaly segment and l_i its length. We define the AEP score as:

$$\mathrm{AEP} = \sum_{i=1}^{k} \frac{l_i}{(91 - t_i)^{\alpha}} \tag{12}$$

where $\alpha > 0$ is a proximity decay exponent, typically chosen as $\alpha = 1$ or 2 to balance spatiality and temporality. A smaller $(91 - t_i)$ indicates a segment closer to the earthquake, thereby increasing the score.

To identify strongly significant thermal anomalies, we further define a threshold based on the empirical distribution of AEP scores across a global catalog of 220,182 earthquakes (as shown in Figure S1 in Supplementary File S3). Denoting AEP_i as the anomaly emphasis proximity score for the ith event, we define the strong significance criterion as:

$$\mathrm{event}_{\mathrm{strong}} : \mathrm{AEP}_j \geq \mathrm{AEP}_{\mathrm{strong}} = \mathrm{Median}\left(\left\{\mathrm{AEP}_j\right\}_{j=1}^{220{,}182}\right) \tag{13}$$

An event is said to exhibit strongly significant thermal anomalies if its AEP score satisfies. This definition emphasizes not only the presence of anomalies but their relative spatiotemporal concentration and recurrence strength compared to the global empirical background. It allows for robust comparison and classification of events based on a unified and physically interpretable metric.

Similarly, the AEP Score Post the earthquake is shown below,

$$\mathrm{AEP}_{\mathrm{post}} = \sum_{i=1}^{k} \frac{l_i}{(31 - t_i)^{\alpha}} \tag{14}$$

A higher $\mathrm{AEP}_{\mathrm{post}}$ value indicates that thermal anomalies are more concentrated near the immediate aftermath of the earthquake and persist over consecutive days. Isolated or delayed anomalies receive smaller weights. This metric may capture delayed thermal adjustments or surface responses in seismically active regions.

In summary, we propose a comprehensive physically constrained framework that couples four diffusion-based parameters with annual energy-balance constraints to filter non-tectonic noise. An AEP-based weighting scheme is then employed to explicitly quantify the spatiotemporal persistence of thermal anomalies associated with seismic activity. Specifically, the AEP metric functions as a spatiotemporal filter that amplifies persistent anomalies occurring in close spatiotemporal proximity to the seismic event, while suppressing isolated or distant signals.

3. Results

3.1. Spatiotemporal Response Characteristics of Seismic Thermal Anomalies

The spatiotemporal response characteristics of 220,182 seismic thermal anomalies were extracted using Model 2 (Figure 3). Other model parameters can be found in Supplementary File S4.

A higher correlation indicates that the model more accurately represents real-world temperature dynamics. In Figure 3, inland regions such as TIB, the eastern NWS, ECA, and WCA exhibit moderate fitting accuracy, while several islands in the western Pacific within the SEA region show lower accuracy. In contrast, most other land and oceanic areas maintain high fitting performance, suggesting that the unified model parameters are globally applicable and ensure a reasonable level of comparability across experiments.

Elevated SU values are observed over the Tibetan Plateau and the western Andes, areas characterized by complex high-altitude terrain with extensive mountains, glaciers, and ice sheets, representing some of the most tectonically active regions globally. These conditions

suggest that strongly coupled land–atmosphere interactions may amplify spatiotemporal variability. Although localized perturbations occur elsewhere, the overall SU distribution remains within a relatively low range.

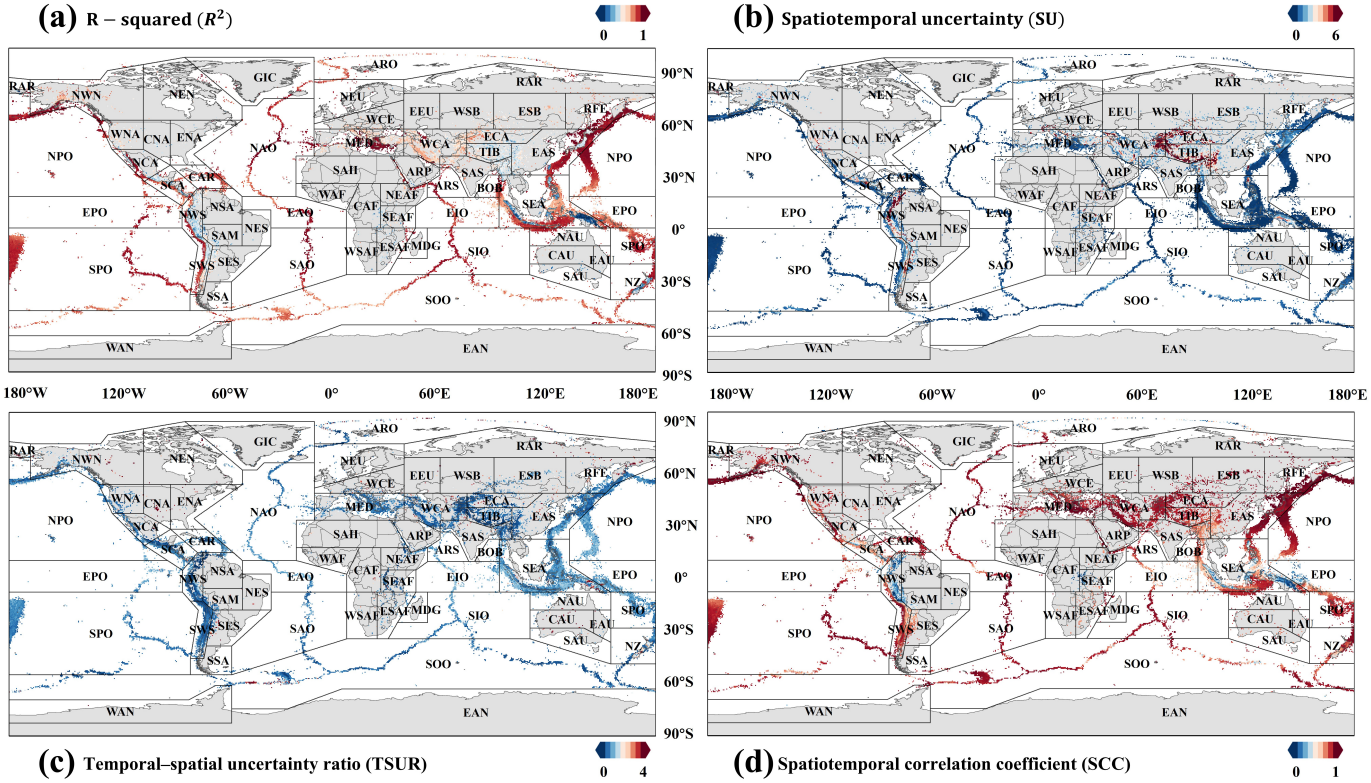


Figure 3. Spatiotemporal Patterns of Seismic Thermal Anomaly Responses (R^2, SU, TSUR, SCC).

TSUR > 1 indicates dominant temporal uncertainty, suggesting enhanced temporal variability and possible time-pattern irregularities. Therefore, this index serves as an indicator of flux rates in coupled atmosphere–land–ocean systems. Notable regions with elevated TSUR values include southeastern Southeast Asia (particularly Papua New Guinea), northern RFE, several high-latitude and polar regions such as RAR, NWN, CNA, and ARO, as well as the eastern Drake Passage between Cape Horn and Antarctica. Although TSUR partially reflects coupling intensity by definition, from a time-series perspective, higher values may correspond to an increased likelihood of detecting thermal anomalies. However, such anomalies are not always physically interpretable; rapid temperature changes in regional fields may arise from transient subsurface heat sources or vigorous atmospheric convective heat exchange.

Except for certain equatorial and coastal regions (e.g., SEA, EPO, NWS, CAF, and SEAF), most areas exhibit high local temporal coherence. According to the interpretation of the thermal penetration index, localized decorrelation often signifies the presence of non-concentrated transient heat sources, suggesting spatially incoherent local disruptions. The aggregation of such anomalies near the equator likely reflects regionally driven processes associated with strong climatic variability, possibly linked to distinct atmosphere–land–ocean coupling regimes that facilitate abrupt energy exchanges across system boundaries. Moreover, apart from the persistently low values over SEA and SCA—both regions of complex ocean–land interaction—most terrestrial and marine surfaces maintain consistently high spatiotemporal correlation coefficients over multiple years.

In summary, the collective spatiotemporal behavior of these four parameters suggests that regions exhibiting strong responses may be influenced by deeper and potentially

transient subsurface heat sources. The spatial and temporal trajectories of these parameters differ markedly, underscoring the inherent complexity of temperature field dynamics within global seismically active zones.

Furthermore, by examining the temporal evolution of regional patterns in land surface temperature (LST) and sea surface temperature (SST) across six representative IPCC regions over a 15-year period, the spatiotemporal response characteristics of surface and oceanic thermal anomalies were further analyzed. In Figure 4, the SU values of oceanic surfaces generally remain lower and more stable over time, except for notable disturbances observed in the SWS region around 2014 and a transient fluctuation in the EAS region between 2010 and 2011. In contrast, the SU values over land surfaces are typically higher and exhibit lower temporal stability. Particularly, a pronounced surface anomaly was detected in the RFE region in 2006, while the TIB region showed recurrent fluctuations throughout the entire time series.

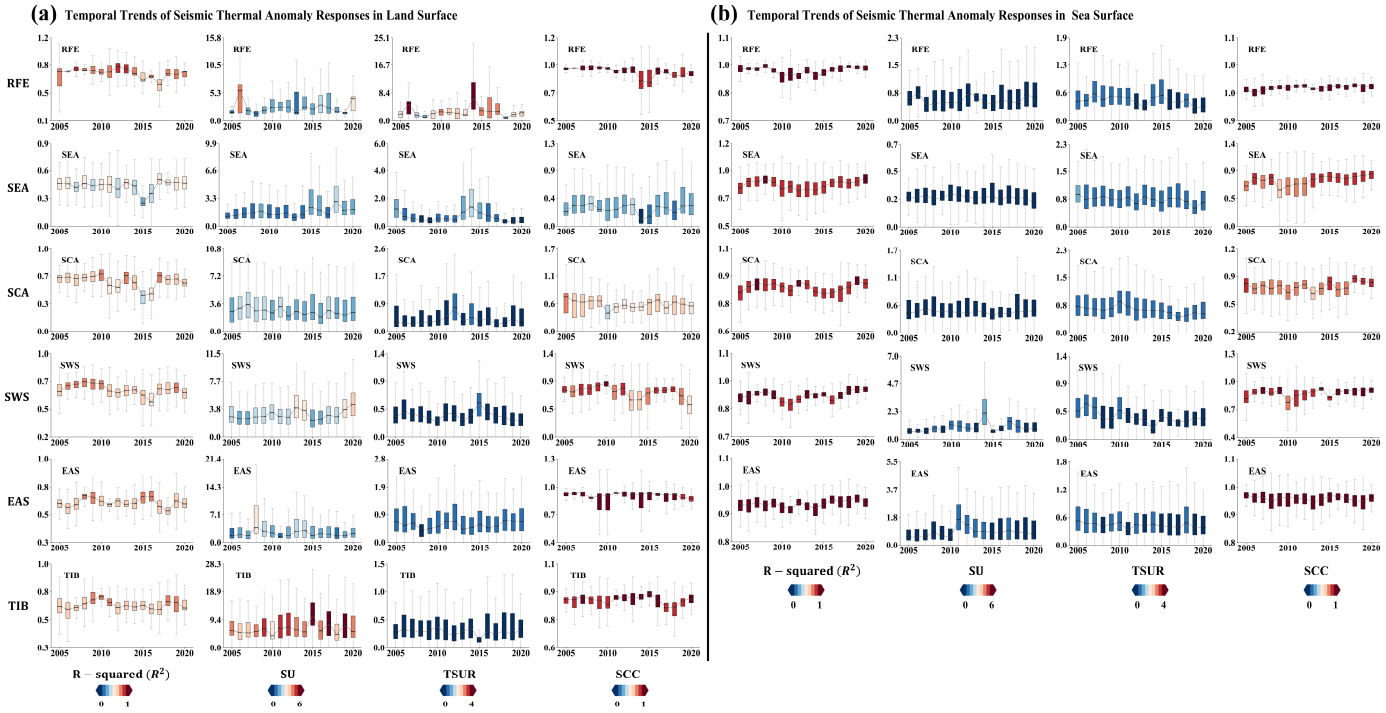


Figure 4. Temporal Trends of Seismic Thermal Anomaly Responses in Land and Sea Surface Temperatures for Representative IPCC Regions.

With the exception of distinct variations detected around 2004 in the land surfaces of the RFE and SEA regions, most domains exhibited relative stability from 2005 to 2020. The long-term mean of this ratio across all regions remains below unity, indicating that spatial uncertainty generally predominates over temporal uncertainty. Lower values reflect stronger spatial heterogeneity, underscoring the necessity of high-resolution surface observations. In such regions, the use of coarse-resolution data could obscure spatial complexity and introduce biases in anomaly detection results. Consequently, this finding validates our selection of 1 km resolution for land surface temperature and 5 km resolution for sea surface temperature as the baseline inputs.

3.2. Spatiotemporal Evolution of Positive, Negative, and Mixed Thermal Anomalies Before and After Earthquakes

To systematically investigate the spatiotemporal evolution patterns of seismic thermal anomalies, this study conducted a comprehensive comparative analysis of the spatial distribution and correlations of positive, negative, and mixed thermal anomalies before

and after earthquakes, across different temporal intervals (2005–2012 and 2013–2020), land–sea locations, and representative IPCC regions (Figure 5). The global analysis reveals that thermal anomalies are not uniformly distributed but are highly concentrated along the Himalaya–Circum-Pacific tectonic belts. At the IPCC regional scale, distinct spatial differentiation is evident among anomaly types.

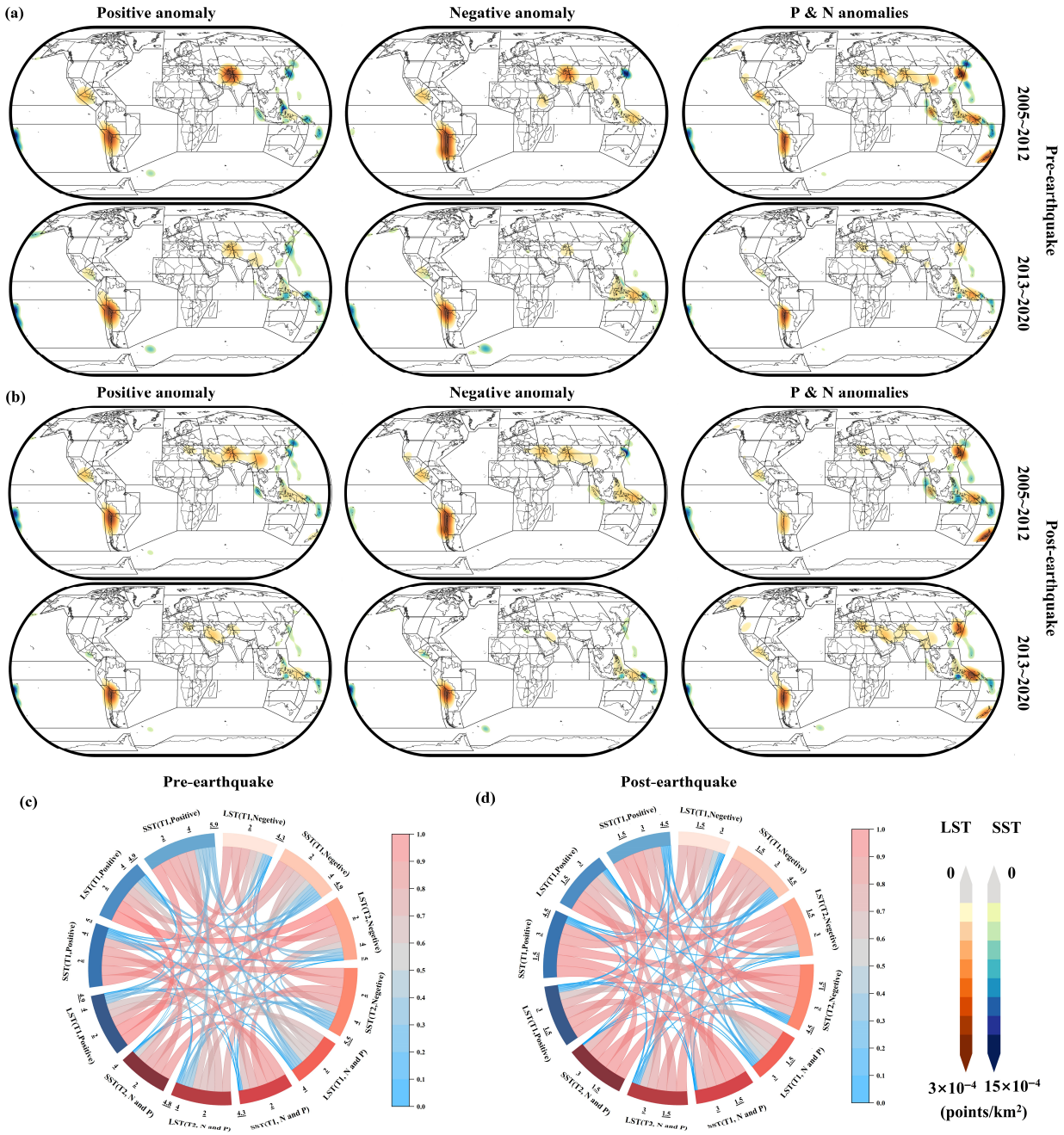


Figure 5. Spatial Distribution and Correlation Comparisons of Positive, Negative, and Mixed Thermal Anomalies. (**a**) Global distribution of positive, negative, and mixed (P&N) anomalies during the two pre-earthquake periods; (**b**) Global distribution of positive, negative, and mixed anomalies during the two post-earthquake periods; (**c**) Correlation analysis of positive, negative, and mixed anomalies during the two pre-earthquake periods; (**d**) Correlation analysis of positive, negative, and mixed anomalies during the two post-earthquake periods.

For instance, within the Tibetan Plateau (TIB), an evident east–west contrast is observed: the central and eastern subregions (e.g., TIB-01, TIB-02) tend to exhibit negative or mixed anomalies, whereas the western subregion (TIB-03) displays all three types, with positive anomalies predominating in both frequency and spatial extent. Similarly, along the western coast of South America, the Andean region (SWS) demonstrates the coexistence of all three anomaly types. A representative case of land–ocean interaction is found around Papua New Guinea, encompassing both the Southeast Asia (SEA) and the Equatorial. Pacific-Ocean (EPO) regions. Here, sea surface temperature (SST) anomalies are predominantly positive, while land surface temperature (LST) anomalies are mostly negative, revealing a potential land–ocean thermal contrast mechanism.

These spatial patterns collectively indicate that local geological structures, surface properties, and regional climatic backgrounds exert profound regulatory influences on the characteristics of thermal anomalies.

Correlation analysis based on chord diagrams further reveals the complex interdependencies and evolutionary relationships among different types of thermal anomalies across time periods (Figure 5). The results show that, compared with 2005–2012, the association networks formed by SST and LST anomalies during 2013–2020 exhibit a more systematic and extensive structure. Within this correlation network, mixed positive–negative anomalies occupy a central hub position, suggesting that such events may possess the highest spatial coherence and the strongest land–ocean coupling intensity. The prominence of this later-stage structure also highlights the distinctiveness of the extreme anomaly cluster observed earlier (2005–2012) over the Japanese Islands (EAS region), which abruptly disappeared in the following period—implying a possible phase transition in the regional thermal anomaly background field. In contrast, low correlation values mainly occur between anomalies of opposite polarity within the same period or between different types of anomalies (e.g., LST vs. SST) across different periods, potentially indicating the occurrence of polarity transitions (from positive to negative or vice versa). Overall, the more robust and complex correlation network observed in the later period may reflect enhanced spatial aggregation of thermal anomalies or a stronger influence from large-scale external drivers, such as interdecadal climate oscillations.

The temporal dimension of thermal anomaly distribution exhibits pronounced dynamic evolution. A comparison between the two periods (2005–2012 vs. 2013–2020) reveals clear shifts in dominant anomaly types across multiple IPCC regions. A notable example is found along the western Andes (SWS region), where early-stage anomalies were dominated by negative types with higher spatial clustering and broader coverage, transitioning to positive anomalies that became more prominent in both density and extent during the later stage. From the perspective of pre- and post-earthquake variations, a general trend emerges: the proportion of mixed anomalies significantly decreases after earthquakes, reflecting a shift from a pre-earthquake mixed mode toward a post-earthquake polarized dominant mode. However, in certain regions, such as Papua New Guinea (SEA and EPO), the frequency of post-earthquake anomalies even surpasses that of the pre-earthquake stage, suggesting that seismic events may trigger or amplify local land–atmosphere–ocean coupling processes.

Collectively, these findings demonstrate that seismic thermal anomalies are not static signals but temporally evolving processes intrinsically linked to seismic cycles. This statistical evidence substantiates a non-random physical connection between large-scale seismicity and surface temperature, suggesting that future research must transcend single-event case studies in favor of multi-event, multi-stage statistical frameworks.

As shown in Table 1, three representative inland regions (TIB, SCA, ECA) and three typical coastal–oceanic regions (RFE, CNA, SWS) were selected to examine the spatiotemporal characteristics of positive and negative thermal anomalies.

Table 1. Proportion distribution of positive and negative abnormal frequencies under different parameters.

			LST			SST		
			Negetive	**N and P**	**Positive**	**Negetive**	**N and P**	**Positive**
Pre	TIB	T1	5.3%	92.0%	2.7%			
		T2	5.4%	88.6%	5.9%			
	SCA	T1	18.7%	64.6%	16.8%			
		T2	22.1%	63.6%	14.3%			
	ECA	T1	18.5%	64.8%	16.7%			
		T2	14.3%	69.5%	16.2%			
	RFE	T1	18.8%	61.6%	19.6%	13.9%	71.1%	15.0%
		T2	32.6%	44.5%	23.0%	24.1%	54.9%	21.0%
	CNA	T1	8.9%	76.7%	14.3%	0.1%	99.6%	0.3%
		T2	1.6%	96.3%	2.0%	0.0%	99.0%	1.0%
	SWS	T1	30.6%	52.3%	17.2%	47.2%	35.0%	17.9%
		T2	24.8%	61.6%	13.6%	27.0%	19.8%	53.2%
Post	TIB	T1	22.8%	49.4%	27.7%			
		T2	20.1%	56.4%	23.4%			
	SCA	T1	31.6%	40.3%	28.1%			
		T2	32.7%	40.1%	27.2%			
	ECA	T1	31.2%	35.4%	33.4%			
		T2	23.5%	50.7%	25.8%			
	RFE	T1	34.3%	39.8%	25.8%	35.7%	20.4%	43.9%
		T2	26.0%	44.2%	29.8%	32.4%	22.1%	45.6%
	CNA	T1	13.2%	67.6%	19.2%	0.0%	1.3%	98.7%
		T2	19.3%	63.2%	17.6%	0.0%	40.2%	59.8%
	SWS	T1	45.3%	23.4%	31.3%	62.5%	9.3%	28.2%
		T2	42.1%	26.0%	31.9%	36.0%	6.1%	57.9%

The analysis quantifies the proportional distribution of positive, negative, and mixed (coexisting) anomaly frequencies across two distinct temporal periods (T1: 2005–2012 and T2: 2013–2020). By distinguishing between pre-earthquake and post-earthquake phases, the table reveals the variation in Land Surface Temperature (LST) and Sea Surface Temperature (SST) response patterns.

The results reveal pronounced pre- and post-earthquake transitions. Temporally, the pre-earthquake stage is dominated by mixed anomalies (N and P), with probabilities often exceeding 60%; for instance, the TIB region reaches 92.0%. After earthquakes, this mixed pattern rapidly collapses into a single polarity, typically negative or positive, as observed in the SCA region, where the probability of negative anomalies increases from 18.7% before to 31.6% after earthquakes. Spatially, the responses differ markedly among regions: inland areas exhibit a significant rise in negative anomalies following earthquakes, whereas coastal regions show an overwhelming increase in positive sea surface temperature (SST) anomalies. In the CNA region, SST positive anomalies surge from 0.3% before to 98.7% after seismic events, forming a striking land–sea contrast.

Moreover, from 2013 to 2020, the overall probability of positive anomalies increases substantially—for example, in the SWS region, SST positive anomalies rise from 17.9% to 53.2%—suggesting the modulation of background climatic conditions. Finally, the type of data fundamentally shapes the anomaly pattern: LST tends to exhibit negative responses (e.g., post-earthquake LST negative anomalies reach 45.3% in SWS), whereas SST

consistently presents strong and coherent positive anomalies. Finally, terrestrial surfaces exhibit remarkable consistency between the T1 and T2 periods, whereas sea surfaces display substantial differences across the two periods, with average changes exceeding 15%. This contrast highlights the challenges in accurately reconstructing the thermal background due to the response characteristics of underlying surface properties.

The spatiotemporal variations of positive, negative, and mixed thermal anomalies in land and sea surfaces (Figure 6) reveal differentiated responses across IPCC regions in terms of both surface type and temporal period. Specifically, the frequency of post-earthquake anomalies in land surface temperature (LST) shows an increasing trend in regions such as SAM(2), SAM(3), NWS(1), and NWS(2), whereas it decreases in NCA, SCA(1), RFE(3), and WCA(3). For sea surface temperature (SST), the most pronounced changes occur along the western Pacific coastlines (e.g., NPO, NAU) and the eastern Pacific margins, particularly from SWS(1) to SWS(4). Observations indicate that, compared with the early period (2005–2012), the number of regions exhibiting SST anomalies increases substantially in the later period (2013–2020), whereas the spatial dynamics of negative anomalies follow different trajectories.

In summary, the spatiotemporal evolution of positive, negative, and mixed thermal anomalies transitions from a chaotic pre-earthquake mixed mode to a post-earthquake polarized dominance, revealing the dynamic reorganization of regional thermal stress patterns; this evolution may be driven by local geology, surface properties, and climatic processes. Notably, within this evolution, mixed anomalies, encompassing simultaneous positive and negative events, tend to exert a broader spatial influence than single-type anomalies. However, their frequency concentration demonstrates a marked decline during 2013–2020 compared to earlier periods. This distinct shift in anomaly patterns may reflect enhanced environmental responses and altered system stability against the backdrop of global climate change.

3.3. Spatiotemporal Clustering Characteristics of the Thermal Anomalies Pre- and Post-Earthquake Events

Building upon the distinctive anomaly patterns identified in the preceding chapter across Japan, the Tibetan Plateau and adjacent regions, the Gulf of Mexico, and the Andes Mountains, this chapter subdivides the study period into three narrower intervals for a more systematic analysis of the anomalies. We then compare these refined temporal anomaly patterns with the spatiotemporal distribution of actual seismic events, aiming to elucidate tighter correlations between observed anomalies and earthquake occurrences.

The spatial clustering of positive and negative anomalies indicates the presence of thermal anomalies; however, their statistical correlation with seismic activity remains uncertain. To address this, we introduce the Anomaly Emphasis Proximity (AEP) Score.

In Figure 7, the aggregation characteristics of the AEP are illustrated for four representative regions. First, in the Tibetan Plateau and its surrounding areas, two extensive pre-earthquake anomaly clusters existed between 2005 and 2010, one in the west and one in the east. Over time, these clusters gradually diverged: the western cluster shifted westward while contracting, whereas the eastern cluster migrated southwestward across China at an approximate rate of 100 km per year. Second, in southern Central America (SCA) and adjacent regions, the first two periods were dominated by prominent clusters of land surface temperature (LST) anomalies, whereas during 2016–2020 the clustering abruptly shifted to sea surface temperature (SST) anomalies, exhibiting a pattern of initial intensification followed by decline, potentially reflecting a phase change in the region's land–ocean–atmosphere coupling dynamics. Third, in eastern Japan and the Russian Far East (RFE), enhanced pre-earthquake thermal anomaly clusters appeared in the Northeast Asia corner during 2011–2015, followed by a rapid decline in 2016–2020.

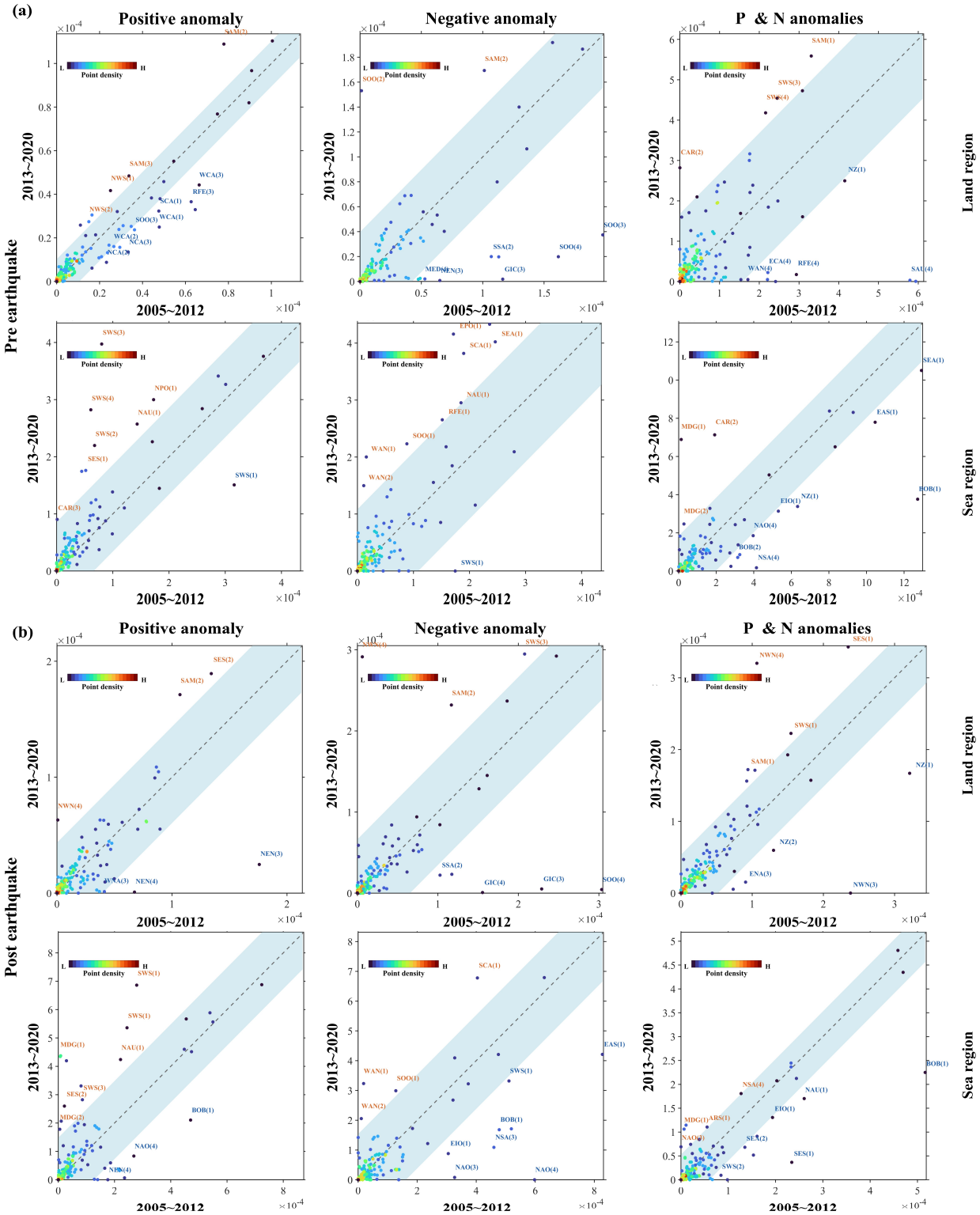


Figure 6. Temporal and Spatial Variations of Positive, Negative, and Mixed Thermal Anomalies in Land and Sea Surface Temperatures. (**a**) Spatiotemporal dynamic variations of positive, negative, and mixed thermal anomalies in land (top three rows) and sea (bottom three rows) surface temperatures during the two pre-earthquake periods; (**b**) Spatiotemporal dynamic variations of positive, negative, and mixed thermal anomalies in land (top three rows) and sea (bottom three rows) surface temperatures during the two post-earthquake periods.

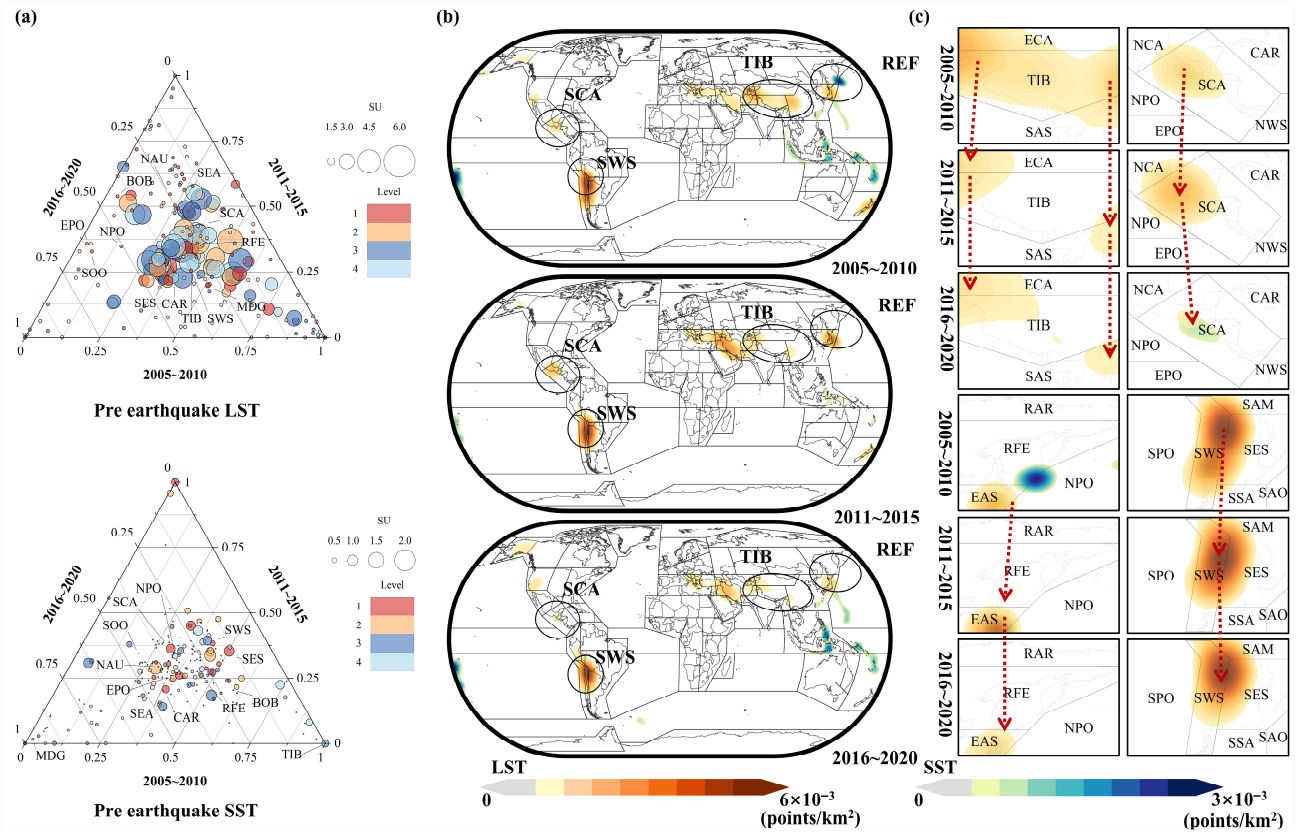


Figure 7. Spatiotemporal Clustering of Significant Pre-earthquake AEP Indices in Land and Sea Surface Temperatures. (**a**) Ternary phase diagrams of spatiotemporal clustering of significant pre-earthquake AEP indices in land (LST) and sea (SST) surface temperatures during three time periods; (**b**) Spatial distribution of spatiotemporal clustering of significant pre-earthquake AEP indices in land and sea surface temperatures during three time periods; (**c**) Spatial distribution changes of typical regions for spatiotemporal clustering of significant pre-earthquake AEP indices in land and sea surface temperatures during three time periods.

Additionally, high-frequency SST anomaly clusters were observed during 2005–2010 but did not recur in subsequent periods, suggesting the presence of region-specific processes at that time. Fourth, in southwestern South America (SWS), AEP clusters in all three periods were concentrated along the western margin of the Andes subduction zone; during 2005–2010, the cluster extended southward, while the core anomalous area persisted throughout the study period, consistent with the frequent occurrence of high-magnitude seismic events in the region.

Post-earthquake comparison (Figures 7 and 8) indicates that the aggregation characteristics of the AEP in four representative regions exhibit pronounced spatiotemporal differentiation. In the TIB region, post-earthquake responses diverge between east and west, with the eastern cluster expanding and exhibiting a delayed response, while the western cluster weakens significantly. In SCA, the pattern shifts from a pre-earthquake land–ocean-dominated anomaly to a sustained post-earthquake thermal release. The RFE region displays heterogeneous thermal responses, with some anomalies persisting and others rapidly decaying. In contrast, the SWS region maintains a highly consistent pre- and post-earthquake pattern, reflecting the dominant influence of a stable structural background. These results reveal that the impact of earthquakes on AEP patterns is strongly region-specific.

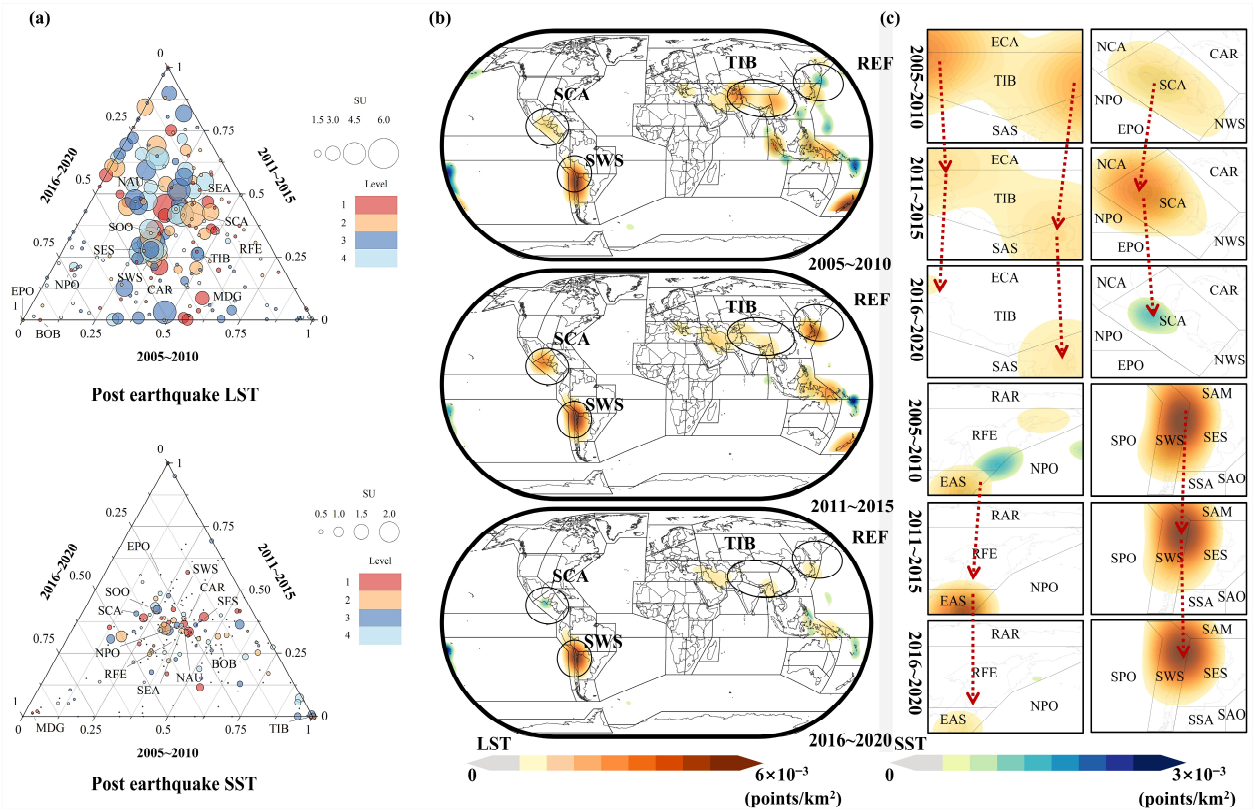


Figure 8. Spatiotemporal Clustering of Significant Post-earthquake AEP Indices in Land and Sea Surface Temperatures. (**a**) Ternary phase diagrams of spatiotemporal clustering of significant post-earthquake AEP indices in land (LST) and sea (SST) surface temperatures during three time periods; (**b**) Spatial distribution of spatiotemporal clustering of significant post-earthquake AEP indices in land and sea surface temperatures during three time periods; (**c**) Spatial distribution changes of typical regions for spatiotemporal clustering of significant post-earthquake AEP indices in land and sea surface temperatures during three time periods.

Based on the improved IPCC AR6 regional division and seismic hotspot classification, ternary diagram analyses (Figures 7a and 8a) reveal the spatiotemporal evolution of pre- and post-earthquake AEP distributions for land and sea surfaces. Pre-earthquake LST AEP clusters are primarily concentrated between 2005 and 2015 and exhibit a significant negative correlation with earthquake frequency, with high-activity regions corresponding to lower thermal background uncertainty (SU). Post-earthquake LST clusters shift temporally to 2011–2020 while maintaining strong coupling with earthquake frequency and SU. In contrast, pre-earthquake SST AEP clusters are concentrated in 2016–2020, with weak correlation to seismic activity, and post-earthquake SST distributions are relatively uniform across three periods, further reducing coupling with earthquakes. These patterns indicate a clear divergence in spatiotemporal distribution and coupling strength between LST and SST, reflecting fundamental differences in the thermal response of land and ocean surfaces to seismic events.

LST anomalies display higher variability and a pronounced temporal shift in dominant aggregation periods post-earthquake, while SST anomalies remain temporally balanced with lower variability. These results highlight the differential influence of underlying surface environments on thermal anomaly clustering and the complexity of pre- and post-earthquake temperature field dynamics in seismically active regions.

3.4. Spatiotemporal Coupling Between Regional Aggregation of the AEP and Earthquake Epicenters

The spatiotemporal clustering of pre-earthquake AEP indices (2005–2020) shows strong correspondence with the spatial distribution of global M ≥ 7 earthquakes, as illustrated in Figure 9. In the Tibetan Plateau, the locations of major earthquakes—including the 7.6-magnitude event in 2005, the 7.5-magnitude event in 2015, and multiple strong shocks in 2008—coincide with areas of high thermal anomaly density. In eastern Japan (EAS), the 9.1-magnitude earthquake in 2011 overlaps spatiotemporally with AEP clusters during 2011–2015. Similarly, in the offshore Russian Far East (RFE), strong SST AEP clusters observed from 2005 to 2010 align with frequent high-magnitude events in the same period, including two M ≥ 7 earthquakes in 2006 and the M8.1 earthquake in 2007, whereas such events are significantly fewer outside this period.

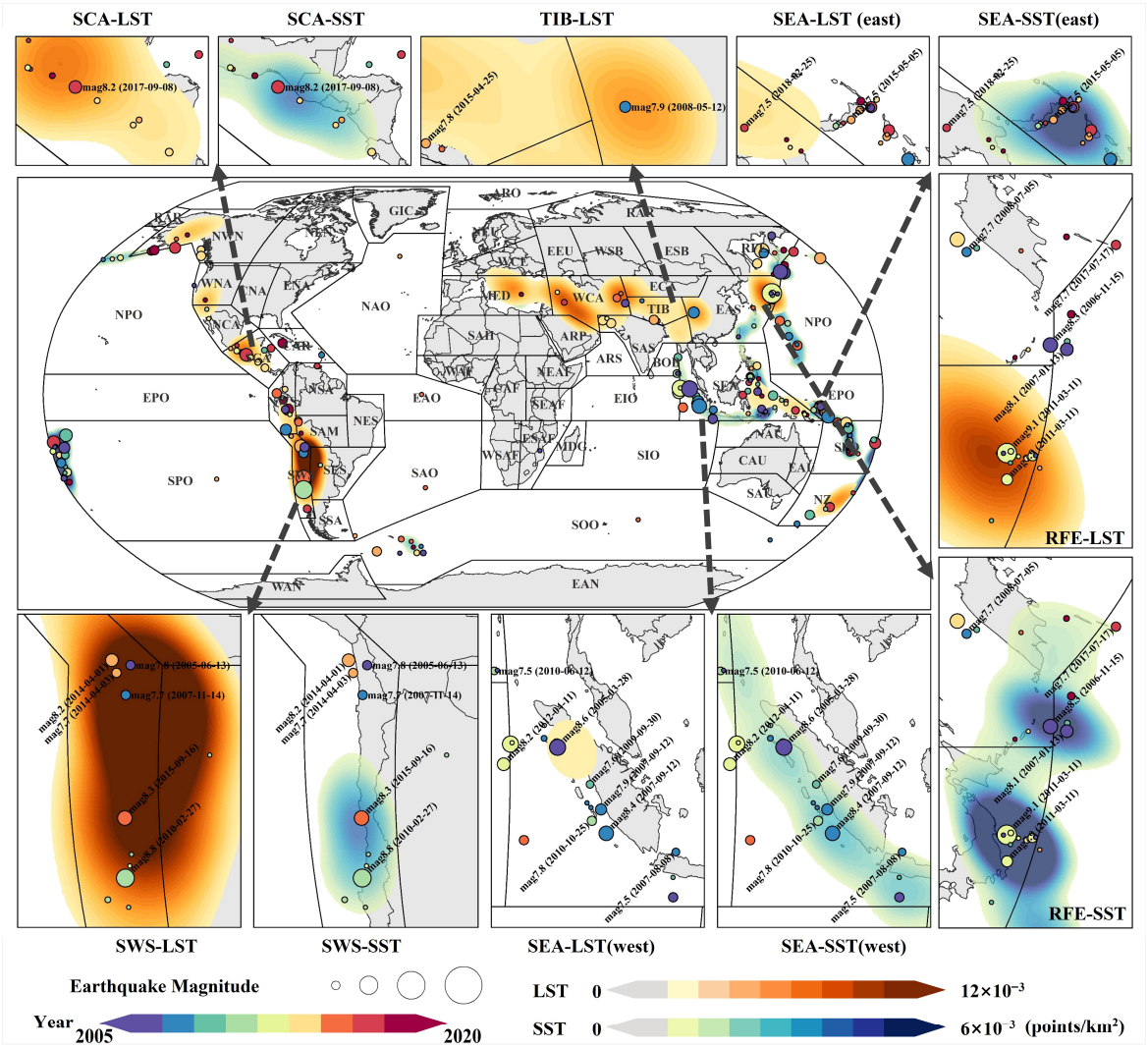


Figure 9. Spatiotemporal Clustering of Significant Pre-earthquake AEP Indices (2005–2020) and Spatial Correspondence with Global M ≥ 7 Earthquakes.

Analysis of Figures 7 and 9 further indicates that the offshore islands along Australia's east coast, as part of the Pacific Rim seismic belt, exhibit relatively low AEP values during 2011–2015, consistent with the few strong earthquakes recorded in this interval (2006–2009, 2016, 2020). Likewise, regions along Southeast Asia (SEA) and the western Pacific seismic belt show temporal synchrony between AEP indices and strong seismic activity.

On the western side of the Andes (SWS), high-density AEP clusters persist throughout the study period, corresponding to annual M $\geq$ 7 earthquakes, with the 8.8-magnitude 2010 earthquake associated with markedly elevated AEP values. In contrast, in the SCA region of the Gulf of Mexico, AEP cluster areas remain stable in the first two periods (2005–2010, 2011–2015) but contract during 2016–2020, despite ongoing strong seismic events, suggesting potential phase-dependent differences in regional energy release processes that warrant further investigation.

In summary, the aggregation characteristics of AEP indices across global regions (Figure 9) show high-density clusters observed in areas such as SCA and SWS and relatively sparse distributions in CNA and ECA. This highlights a notable spatial correspondence between AEP clusters and strong seismic activity across multiple tectonic units, preliminarily suggesting the potential seismic relevance of thermal anomalies. However, analyses based solely on spatial overlap are insufficient to statistically establish an intrinsic link or rule out the possibility of random coincidence.

To ensure the robustness of the findings, this study incorporates non-seismic thermal anomaly samples (spatiotemporal cubes of AEP alerts, including negative samples in IPCC regions, the flowchart as shown in Figure S9 in Supplementary File S3) and applies the significance testing method proposed by Zhang et al. [82] to systematically evaluate the statistical association between thermal anomalies and seismic activity. The experimental design divides the study period into three temporal segments (2005–2010, 2010–2015, 2015–2020) to assess the influence of temporal scale, and selects four representative high-density regions (SCA, SWS, RFE, TIB) and two low-density regions (CNA, ECA) to reveal the spatiotemporal heterogeneity and dependency of the anomaly–earthquake relationship. Across all regions, thermal anomalies passed significance tests ($p_1 \leq 0.05$, $p_2 \leq 0.05$), with optimal detection parameters of M = 4, T = 50 days, D = 75 km for CNA, ECA, and TIB, and M = 4, T = 50 days, D = 100 km for RFE, SCA, and SWS.

As shown in Table 2, the significance test was conducted in two cross-validation steps. First, the T1 period was used for training and the T2 period for validation to obtain the initial set of p-values. Then, the T2 period served as the training window and the T3 period as the validation window to generate the second set of p-values. For each of the three periods, the corresponding significance indicators were computed using the optimal detection parameters derived from these training procedures.

The association between thermal anomalies and seismic activity exhibits pronounced spatial heterogeneity and temporal stability. In high-density regions (e.g., SCA and SWS), the false discovery rate (FDR) remains low (10.5–18.5%), indicating high alert reliability, while the false negative rate (FNR) is also low (4.0–17.8%), reflecting effective omission control. Elevated STCW values (3.7–12.6%) indicate broad alert coverage, and low loss values (0.10–0.13) confirm overall superior performance. In contrast, low-density regions (e.g., CNA and ECA) show extremely low FNR (0.0–19.8%) but relatively high FDR (33.1–61.5%), suggesting frequent false alarms; small STCW values (0.1–1.9%) reflect overly concentrated alerts, leading to moderate loss values (0.19–0.36).

Specifically, the RFE region exhibits a unique "high-reliability, high-miss" pattern (FDR 23.1–30.2%, FNR 36.7–63.1%), likely due to complex seismic mechanisms or weak thermal signals. In contrast, the TIB region demonstrates moderate association strength, potentially influenced by high-altitude background signal-to-noise characteristics. All cases pass significance testing (Type I alert), confirming the statistical linkage between algorithm-detected thermal anomalies and earthquakes. However, the association strength displays clear regional dependency: it is strong and stable in high-density regions (e.g., SCA and SWS, with minimal temporal fluctuations) and weaker and more variable in low-density regions (e.g., CNA, where FDR sharply declines in the T2 period).

Table 2. Significance test index values in typical regions at different times.

Significance Test	*p*1-Value	*p*2-Value	FDR	FNR	STCW	Loss
CNA-T1	4.8×10^{-10}	2.2×10^{-12}	61.5%	10.0%	0.1%	0.36
CNA-T2	5.5×10^{-10}	3.0×10^{-11}	33.1%	0.0%	0.5%	0.19
CNA-T3			48.1%	0.0%	0.4%	0.28
ECA-T1	7.9×10^{-10}	2.5×10^{-8}	53.3%	15.7%	1.6%	0.32
ECA-T2	2.8×10^{-10}	4.5×10^{-8}	51.1%	13.5%	1.9%	0.31
ECA-T3			49.6%	19.8%	1.7%	0.31
TIB-T1	5.5×10^{-6}	2.9×10^{-9}	48.8%	21.9%	2.2%	0.31
TIB-T2	1.2×10^{-5}	3.7×10^{-8}	50.9%	40.0%	2.2%	0.37
TIB-T3			46.0%	28.8%	2.2%	0.31
RFE-T1	4.1×10^{-8}	3.3×10^{-8}	28.2%	36.7%	1.3%	0.27
RFE-T2	2.4×10^{-8}	8.2×10^{-6}	30.2%	63.1%	1.1%	0.40
RFE-T3			23.1%	60.7%	1.1%	0.37
SCA-T1	1.1×10^{-9}	2.2×10^{-9}	13.2%	12.9%	4.6%	0.11
SCA-T2	2.3×10^{-9}	1.4×10^{-8}	10.5%	12.4%	4.5%	0.10
SCA-T3			14.5%	17.8%	3.7%	0.13
SWS-T1	4.3×10^{-4}	1.8×10^{-8}	18.5%	4.0%	11.8%	0.13
SWS-T2	6.7×10^{-6}	4.7×10^{-8}	12.8%	9.7%	11.8%	0.12
SWS-T3			12.5%	6.4%	12.6%	0.11

The results indicate a statistically significant overall association between thermal anomalies and seismic activity; however, spatial heterogeneity emerges as a key characteristic. This association is strong with high predictive performance in tectonically active regions, whereas it is comparatively weak in stable areas, highlighting the dependence of thermal anomalies as potential earthquake precursors on region-specific geological context and activity patterns.

4. Discussion

The results presented in the preceding section have quantified the statistical correlations between thermal anomalies and seismic events, highlighting the marked performance disparity between tectonically active and stable regions. However, identifying these spatiotemporal patterns represents only the initial step. The observed heterogeneity in the FDR and STCW metrics suggests that these thermal signals are not merely random statistical fluctuations but are governed by underlying geodynamic processes. To transition from phenomenological detection to mechanistic understanding, this section interprets these statistical findings within the physical frameworks of stress accumulation, crustal deformation, and thermal diffusion. Consequently, the subsequent discussion is structured to systematically characterize the dynamic evolution of these thermal signatures, evaluate the methodological robustness of the AEP metric, and elucidate the diverse physical mechanisms driving the observed regional heterogeneities.

4.1. Dynamic Spatiotemporal Signatures in Seismic Thermal Anomalies Detection and Evolution

Previous research applied the multi-year period equilibrium strategy of Model 2 to extract thermal anomalies from 220,182 earthquakes globally, achieving high fitting accuracy ($R^2 > 0.6$) across most regions and enabling adaptive detection of thermal anomalies worldwide. Despite these strengths, the approach relies on fundamental assumptions, namely that temperature variations at any surface point follow periodic patterns, including seasonal cycles, which can be disrupted by sudden heat sources.

Accordingly, this work introduces, for the first time, a dynamic spatiotemporal adaptive estimation approach, establishing four parameters to characterize the spatiotemporal response of thermal anomalies (R^2, SU, TSUR, SCC). By analyzing the spatiotemporal uncertainty of the local thermal field (SU) and the reconstruction capability of the background signal (R^2), the method captures the complexity of the target region's background, dynamically removes periodic variations, and defines stable boundary values for reconstructing the temporal temperature field.

Although established methods such as RST have demonstrated effectiveness in detecting thermal anomalies within specific regions [42,66], the analysis indicates that anomaly detection is highly dependent on the reconstruction of the background signal. When applying a "global threshold" in complex tectonic regions, such as the Tibetan Plateau, the weakened ability to reconstruct the background signal systematically leads to underfitting (Model 1) or overfitting (Model 3).

Spatiotemporal statistical analysis of positive and negative thermal anomaly samples associated with earthquakes reveals distinct evolutionary patterns. During the pre-earthquake stage, mixed positive and negative anomalies dominate (e.g., N and P anomalies account for 92.0% in the TIB), reflecting competition among multiple heat sources. In the post-earthquake stage, anomalies shift toward a single dominant polarity, terrestrial areas tend to exhibit negative anomalies (post-earthquake negative anomaly probability of 45.3% in SWS-LST), whereas oceanic regions show bursts of positive anomalies (probability in the CNA rises from 0.3% to 98.7%). This land–ocean differentiation highlights the substantial influence of the underlying surface properties on thermal anomaly responses.

Previous studies often present fragmented or even contradictory findings, with some focusing on positive anomalies [31] and others on negative anomalies [32]. The "mixed-to-polarized" pattern revealed here helps reconcile these apparent discrepancies in the literature. Moreover, this transition may reflect the disruption of the critical balance between heat and cold sources during seismic energy release, offering a novel perspective for the identification of precursor signals.

The AEP (Equations (10)–(14)) integrates anomaly persistence and pre-earthquake characteristics to effectively identify significant thermal anomaly events and to examine their spatiotemporal differentiation in terms of spatial clustering. These significant clusters (Figures 7–9) closely correspond to major seismic events, including the 2008 M8.0 earthquake on the Tibetan Plateau (TIB), the 2011 M9.1 earthquake in eastern Japan (RFE), and frequent M7+ events along the western Andes (SWS). The AEP essentially quantifies pre-earthquake heat flux enhancement, with high values consistent with fault pre-slip heating models in which accelerated stress release generates frictional heat. The eastward migration of AEP clusters on the Tibetan Plateau, at approximately 100 km per year, may reflect crustal stress propagation pathways, while persistent AEP clustering along the western Andes may correspond to locked subduction zones. Significance testing that includes negative anomaly samples (p_1, $p_2 < 0.05$) confirms that these associations are not random. In tectonically active regions (SCA/SWS), FDR is less than 18.5%, and STCW exceeds 3.7%, whereas in stable regions (CNA/ECA), FDR exceeds 33.1% and STCW is below 1.9%, indicating that the intensity of thermal anomaly clustering is likely influenced by the underlying structural background.

In summary, by integrating heat-diffusion-derived diagnostic parameters, annual energy-balance constraints, and the AEP scoring scheme, this study constructs a physically constrained framework to capture the dynamic evolution of seismic thermal anomalies. These stages form a sequential, mutually reinforcing process that establishes a closed-loop workflow—transitioning from physically grounded signal capture, to background-noise suppression, and ultimately to the quantitative characterization of thermal anomalies.

This integrated structure significantly enhances both the robustness and interpretability of identifying precursor thermal disturbances in complex surface environments.

4.2. Advantages and Limitations of the AEP Metric

A pervasive challenge across data-driven anomaly detection methodologies is that outputs are frequently manifested as fragmented, discrete temporal markers. The AEP metric was specifically conceived to address this limitation. By quantifying the persistence and temporal proximity of thermal disturbances, AEP serves as a discriminator, effectively segregating genuine tectonic thermal activities from stochastic background noise, such as extreme weather events or wildfires. The primary merit of AEP lies in its integrative capacity: it consolidates discrete time-series anomalies into a coherent scalar metric that reflects both physical consistency and regional discriminative power.

Our results demonstrate that high AEP scores align closely with the fault pre-slip heating model [83,84], effectively capturing the enhanced heat flux associated with accelerated stress release. This physical validity is empirically corroborated by significance testing: in tectonically active zones like the Western Andes (SWS), AEP maintains a False Discovery Rate (FDR) below 18.5%, a performance significantly superior to that in stable regions (>33.1%). This marked contrast underscores the robustness of the AEP metric in isolating authentic tectonic signals against complex geological backgrounds.

Notwithstanding the aforementioned strengths, the AEP metric, as a temporal weighting system, remains susceptible to extreme non-tectonic disturbances. While the upstream annual energy-balance constraints effectively suppress routine solar and seasonal variations, the AEP algorithm is mechanistically predisposed to amplify any signal exhibiting "continuity and density". Consequently, prolonged meteorological anomalies—such as multi-week heatwaves or persistent atmospheric blocking—that bypass the initial physical filters could theoretically result in the spurious inflation of AEP scores. To mitigate this, future iterations of this framework would benefit from integrating finer-scale atmospheric dynamic models as secondary filters, thereby further isolating subtle pre-earthquake thermal signatures from extreme weather masking.

Beyond climatological factors, the heterogeneity of tectonic settings necessitates careful consideration. The manifestation of thermal signals—specifically their distinct weights in persistence and urgency—is heavily modulated by local geological attributes, such as fault geometry and geomorphology. A "one-size-fits-all" weighting scheme may not capture these nuances across diverse terrains. Therefore, future research aims to incorporate comprehensive geodynamic parameters to enable site-specific calibration of these weighting factors, thereby enhancing the adaptability of the metric to complex crustal environments.

4.3. Underlying Mechanisms Behind Regional Differentiation

4.3.1. Typical Multi-Sphere Coupling Mechanisms in Thermal Anomaly Evolution

To interpret the spatiotemporal dynamics of thermal anomalies presented in Figures 7 and 8, we employ a multi-sphere interaction framework, specifically the Lithosphere-Ocean-Atmosphere Coupling, to determine the underlying mechanisms. By analyzing the density clustering dynamics of Pre-earthquake Thermal Anomalies (AEPs) across three distinct tectonic environments from 2005 to 2020, we ascribe the observed spatial heterogeneity to specific geophysical coupling modes.

1. Deep-Ocean Attenuation and Filter Effect (Mid-Atlantic Ridge). Observations indicate a distinct scarcity of significant AEP clusters despite frequent seismic activity in this region. This "muted" response is fundamentally governed by the thermodynamic inertia of the deep ocean. Unlike terrestrial environments, thermal energy generated by seabed stress—whether via fluid convection or degassing—must traverse a

massive water column, undergoing significant attenuation due to the high specific heat capacity of seawater and vigorous circulation. Consequently, this mechanism functions as a "Dissipative Filter". Only thermal anomalies of exceptional intensity and duration can breach this "inertial barrier" to reach the sea surface. This physical constraint elucidates the unique "High-Reliability, High-Miss Rate" pattern observed in deep-sea regions (and the chemically similar RFE zone): while the ocean suppresses weak signals leading to numerous missed detections, any anomaly that successfully breaches this suppression is highly likely to be of genuine tectonic origin. Therefore, the lack of physical uniformity between events in this region reflects sporadic breakthroughs under extreme energy thresholds, highlighting the physical coupling mechanism between the ocean and the atmosphere.

2. Synergistic and Asymmetric Coupling at Land-Ocean Interfaces (Western Pacific and Southeast Pacific). The Western Pacific seismic belt exhibits the most intricate thermodynamic regime. Data reveal that during major seismic events, this transition zone is dominated by a "Superposition Effect," where thermal anomalies are amplified by the convergence of direct terrestrial radiative heating and enhanced latent heat flux from the adjacent ocean. However, this high sensitivity serves as a double-edged sword. The low thermal inertia of the land side leads to rapid responses to atmospheric perturbations, while the ocean side introduces complex fluid dynamics. This interaction not only results in highly concentrated AEP clusters but also introduces non-tectonic background noise. The superposition of the land's high-frequency response and the ocean's dynamic variability renders the region prone to including non-seismic thermal anomalies in detection. This explains why, although the signal intensity is highest here, its spectral purity is lower than in inland regions. This phenomenon reflects intensified energy exchange prior to mainshocks, underscoring the physical coupling mechanisms among the lithosphere, shallow ocean, and atmosphere.
   Compared with the synergistic mode of the Western Pacific, the Andean tectonic belt along the coast of the Southeast Pacific presents an obvious 'asymmetric interface coupling' mode. Despite the Andes being located at a similar land–sea boundary, it shows a persistent high-density AEP accumulation center on the continental side, which forms a sharp contrast with the relatively weak thermal response of the neighboring ocean. This difference emphasizes that despite its location at the interface, the huge stress accumulation of the subduction zone leads to a coupled response, in which the land component clearly dominates the ocean component. However, this ground signal is obviously stronger than in pure inland areas (such as the Tibetan Plateau). This amplification means the ocean might have produced a thermodynamic contribution through moisture transport. Although the sea surface itself maintains thermal stability, the continuous transfer of water vapor to the high-altitude Andes helps to enhance latent heat release on land. While the synergy of subduction zone stress and oceanic latent heat significantly enhances the land thermal response, this amplification effect triggers severe signal aliasing and 'multi-event fusion' in earthquake-prone areas, obscuring the identification of clear pre-earthquake thermal anomaly patterns.
3. High-Threshold Lithospheric Coupling and Background Noise (Himalayan Fault Zone). In the Himalayan region, the mechanism simplifies to a direct lithosphere-atmosphere interaction, unbuffered by oceanic factors but modulated by extreme topography and climate. Analysis indicates that the dynamic spatiotemporal uncertainty (SU) of anomaly detection here is significantly higher than in plains or marine regions. This is primarily attributed to the Tibetan Plateau's nature as a compressional tectonic belt, where massive stress accumulation is requisite for rock fracture. Although the absence of industrial noise facilitates the observation of AEP migration,

the low thermal inertia of the land surface renders it extremely sensitive to solar radiation and atmospheric disturbances. While this rapid responsiveness allows tectonic thermal signatures to manifest quickly, it inevitably introduces a high-frequency background noise floor. This thermophysical characteristic rationalizes the observed medium False Discovery Rate (FDR): the noisy thermal background generated by complex terrain tends to mask subtle precursor signals. However, during strong seismic events, as signal intensity far exceeds the background, the spatiotemporal migration trajectory of AEPs along fault lines remains clearly observable (Figure 10), validating the transmissibility of "P-hole" activation and gas leakage effects along the tectonic strike.

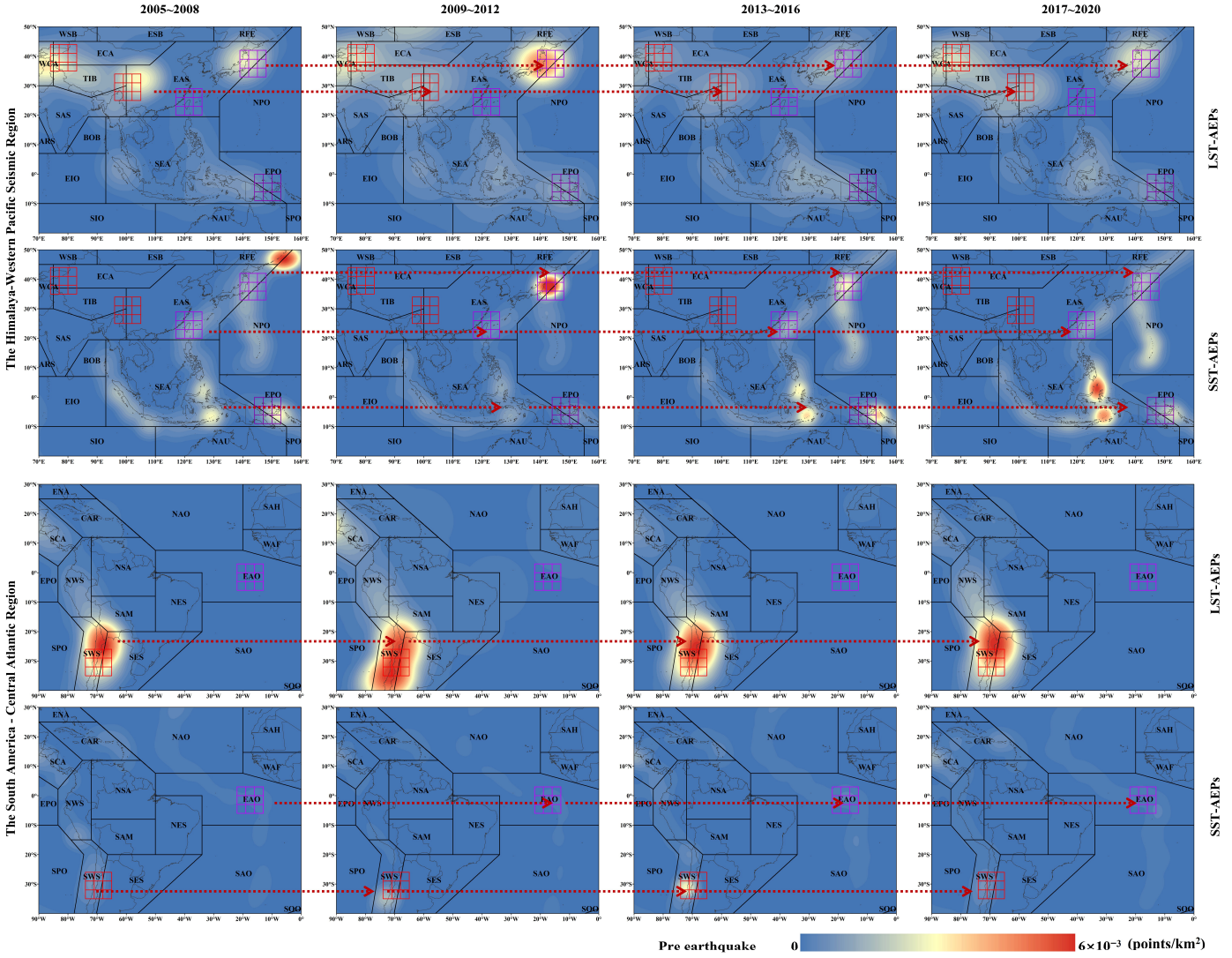


Figure 10. Spatiotemporal evolution of significant Pre-earthquake Thermal Anomaly (AEP) density across two major seismic research zones from 2005 to 2020. The red boxes represent land regions or land-dominated land-sea interfaces, while the purple boxes represent sea regions or sea-dominated land-sea interfaces. The red arrows indicate the spatiotemporal dynamic variations of the same typical locations across different time periods.

In summary, the phenomenon of AEP diffusion weakening on land and strengthening in the ocean, observed in both pre- and post-earthquake phases, further corroborates the coupling of the proposed mechanisms. The distribution characteristics presented in this study are not data artifacts but physical manifestations of varying thermal inertia environments: ranging from the ocean acting as a "filter" for signal shielding, to the signal amplification and aliasing caused by "superposition" at the land–sea interface, and finally to the rapid response and high background thresholds driven by "low inertia" in high-altitude terrestrial zones. These findings underscore that the detectability of seismic thermal anomalies is strictly constrained by the thermodynamic properties of the regional geophysical environment.

4.3.2. Statistical Dependency on Earthquake Types and Focal Depths

To ensure the statistical robustness of our analysis, this study utilizes a comprehensive global catalog comprising 220,182 seismic events ($mag \geq 4$) spanning the past two decades. The dataset is heavily dominated by three primary magnitude scales: body-wave magnitude (m_b, 183,392 events), moment magnitude (M_w, 26,520 events), and local magnitude (M_l, 4635 events). Collectively, these categories constitute 97.44% of the total records, rendering other types (e.g., m_c, m_d; totaling 5365 events) statistically negligible. Geographically, the seismicity is concentrated within oceanic and coastal transition zones (165,238 events), with inland continental events comprising 24.95% (54,944 events). Given this heterogeneous baseline, it is imperative to ascertain whether the detectability of thermal anomalies exhibits specific biases towards certain seismic characteristics across differing tectonic settings.

We further disaggregated the proportional distribution of significant pre-earthquake AEP signals across representative IPCC regions, categorizing them by earthquake type, magnitude, and focal depth (in Table 3). This analysis uncovers a striking dichotomy in the dependence of thermal anomalies on seismic attributes, broadly characterizing a "shallow dominance" in stable continental interiors versus "deep-source anomalies" in subduction zones.

1. Shallow-source dominance (stable regions): In the majority of regions, thermal anomalies are overwhelmingly associated with shallow earthquakes (<20 km). For instance, in Africa (Land) and the EUROPE (Sea), shallow body-wave magnitude (m_b, mag 4–6) events account for 86.86% and 91.29% of the significant signals, respectively. Given that m_b events constitute the bulk of the global catalog, this high detection rate in stable regions implies that the thermal precursor mechanism is strictly depth-constrained, suggesting that energy from deeper sources likely attenuates rapidly during ascent, failing to induce detectable surface temperature perturbations.
2. Deep-source dominance (subduction zones): Conversely, in subduction-dominated regions such as South America and the Pacific (Land), this pattern is inverted. Despite the global prevalence of shallow seismicity, deeper earthquakes surprisingly account for the vast majority of detected anomalies—72.75% in South America and 85.21% in the Pacific. This significant deviation from the global baseline suggests that in convergent plate boundaries, unique geological architectures allow thermal or material signatures from greater depths to migrate vertically to the surface without total dissipation.

Table 3. Statistical distribution of significant pre-earthquake thermal anomalies across representative IPCC land and sea regions, categorized by earthquake magnitude type (m_b, M_w, M_l), magnitude range, and focal depth.

Region (Land Portion)	M_w mag 4–6 Low	M_w mag 4–6 High	M_w mag ≥ 6 Low	M_w mag ≥ 6 High	m_b mag 4–6 Low	m_b mag 4–6 High	M_l mag 4–6 Low	M_l mag 4–6 High	Other
AFRICA	6.73%	1.28%	0%	0%	86.86%	1.92%	2.88%	0%	0.32%
ASIA	4.72%	5.29%	0.54%	0.28%	40.99%	47.57%	0.37%	0%	0.25%
CENTRAL-AMERICA	5.87%	4.95%	0.50%	0.67%	15.18%	34.90%	4.70%	0.17%	33.05%
EUROPE	8.51%	7.45%	0%	0%	29.79%	28.72%	17.02%	2.13%	6.38%
EUROPE-AFRICA	13.64%	2.37%	0.71%	0.24%	58.24%	9.25%	9.49%	1.19%	4.86%
NORTH-AMERICA	37.64%	9.53%	0.81%	0.16%	5.01%	5.49%	33.76%	5.98%	1.62%
OCEANIA	5.95%	3.69%	0.36%	0.36%	15.71%	17.86%	24.40%	11.79%	19.88%
PACIFIC	0%	7.04%	0.70%	2.11%	4.93%	85.21%	0%	0%	0%
SOUTH-AMERICA	0.89%	12.86%	0.10%	1.02%	4.47%	72.75%	0.38%	2.65%	4.87%
Region (Sea Portion)									
AFRICA	10.00%	0%	0.19%	0%	88.49%	0.57%	0.19%	0.19%	0.38%
ARCTIC	6.64%	0.41%	0.41%	0%	91.29%	1.24%	0%	0%	0%
ASIA	2.76%	6.62%	0.30%	0.58%	20.11%	69.10%	0.15%	0.02%	0.36%
CENTRAL-AMERICA	4.75%	3.64%	0.76%	0.31%	27.98%	40.61%	0.90%	0.28%	20.78%
EUROPE	18.37%	0%	2.04%	0%	73.47%	2.04%	4.08%	0%	0%
EUROPE-AFRICA	7.61%	2.68%	0.49%	0.24%	51.52%	25.27%	7.43%	2.13%	2.62%
INDIAN	9.60%	0.88%	0.40%	0.13%	75.26%	13.73%	0%	0%	0%
NORTH-AMERICA	24.74%	12.82%	1.67%	0.64%	24.36%	24.10%	4.62%	6.79%	0.26%
OCEANIA	4.32%	2.31%	0.43%	0.30%	26.81%	33.07%	12.64%	8.94%	11.19%
PACIFIC	4.43%	4.92%	0.69%	0.65%	30.60%	58.15%	0.21%	0.19%	0.17%
POLAR	15.58%	0.36%	0.36%	0%	82.61%	0.36%	0.36%	0%	0.36%
SOUTH-AMERICA	12.35%	9.41%	0.65%	0.69%	22.35%	46.04%	1.78%	4.29%	2.43%
SOUTHERN	9.91%	2.94%	1.45%	0.07%	59.85%	25.77%	0%	0%	0%
ATLANTIC	17.16%	0.27%	1.12%	0%	77.18%	1.02%	0.27%	0.05%	2.94%

Note: In the type row of the table, "low" and "high" are surface source depths, and the boundary is set at 20 km underground to distinguish between shallow and deep source earthquakes.

4.3.3. Coupling of Seismic Characteristics with Physical Thermal Mechanisms

Synthesizing the observed statistical dependencies with established physical models, we hypothesize that the detected thermal anomalies are driven by two distinct, region-specific mechanisms: frictional heating (the shallow/stable regime) and fluid/gas advection (the deep/subduction regime).

1. Local frictional heating (shallow mechanism): In stable regions like Africa, the dominance of shallow m_b events is strongly consistent with the local frictional heating model [84]. The limited transmission distance allows thermal energy generated by micro-fracturing and frictional slip within the shallow crust to diffuse effectively to the surface without total attenuation.
2. Advective transport via fluid/gas migration (deep mechanism): Conversely, the high incidence of anomalies associated with deep-focus events (>20 km) in South America implies a transport mechanism significantly more efficient than pure thermal conduction. We attribute this phenomenon to advective heat transport driven by fluid and gas migration [85,86]. Subduction zones are inherently rich in volatiles. Enhanced stress at depth can drive the upwelling of fluids along high-permeability slab interfaces, acting as a carrier system that transports deep-seated thermal energy to the surface. This mechanism provides a robust explanation for the detectability of anomalies in these regions, even when originating from deep-seated sources.

Fundamentally, the validity of these mechanism differences rests upon the established link between seismic activity and the detected thermal anomalies. By employing a detection framework grounded in interpretable physical processes—rather than purely black-box statistics—we not only enhance the robustness of this association but also provide the necessary empirical scaffolding to substantiate these region-specific geodynamic interpretations.

4.4. Challenges and Future Perspectives

Despite the establishment of an adaptive detection framework, limitations regarding methodological constraints and regional variability persist. Accurate background signal reconstruction remains a critical challenge, as detection sensitivity is compromised by sensor resolution limits, atmospheric interference, and anthropogenic noise. Consequently, subtle pre-earthquake signals may be obscured. Furthermore, data quality uncertainties introduce potential biases into AEP calculations. Most critically, the current analysis remains primarily correlative, necessitating further research to definitively unravel the underlying causal mechanisms.

However, independent time-series analysis of global seismic thermal anomalies reveals a critical yet frequently overlooked aspect in the broader research field, extending beyond the specific scope of our framework. In regions characterized by persistent high-frequency seismicity (e.g., the western Andes, SWS), the spatiotemporal temperature field cubes constructed for two distinct seismic events occurring within a short interval may exhibit significant overlap. This "superposition state" of thermal fields potentially compromises the assumption of regional energy balance (as evidenced by the low R^2 regions in Figure 3a). Consequently, in such complex tectonic settings, it is essential to conduct a preliminary assessment of the framework's background residual separation capability using R^2 prior to proceeding with anomaly extraction and spatiotemporal dynamic analysis.

To advance research toward causal inference, future work should prioritize three key directions. First, the four-parameter system (R^2, SU, TSUR, SCC) should be transformed from static calibration tools into dynamic tracking indicators, capturing temporal evolution to enhance precursor sensitivity. Second, underlying physical mechanisms must be elucidated by simulating the polarity transitions of anomalies and employing cross-validation with non-homologous datasets. Finally, prospective validation should be implemented under multi-physical field constraints—including region-specific parameterization (e.g., α)—and verified through pilot experiments in zones like Sichuan–Yunnan. These efforts aim to elevate thermal anomalies from "auxiliary evidence" to "reliable precursors".

5. Conclusions

To comprehensively assess the spatiotemporal evolution of global seismic thermal anomalies and their response to known seismic activity, an adaptive detection framework rooted in annual energy balance and geospatial constraints is established. By applying four core diagnostic parameters to 220,182 seismic events spanning 2005–2020, the regional adaptability of the detection model was quantified. The results demonstrate that the proposed approach effectively captures the spatiotemporal heterogeneity of thermal anomalies, achieving robust background reconstruction on a global scale ($R^2 > 0.6$).

Distinct evolutionary patterns characterize the polarity of thermal anomalies, shifting from pre-earthquake mixed anomalies to post-earthquake single-polarity dominance, accompanied by pronounced land–ocean differentiation. For instance, post-earthquake sea surface temperature (SST) anomalies increase sharply from 0.3% to 98.7% in coastal regions, whereas land surface temperature (LST) tends to exhibit negative anomalies. Additionally, the introduced Anomaly Emphasis Proximity (AEP) index effectively identifies significant

thermal clusters whose spatial aggregation closely corresponds to major seismic events (e.g., the 2008 Mw 8.0 Tibetan earthquake and the 2011 Mw 9.1 East Japan earthquake). Statistical significance tests incorporating negative samples ($p1$, $p2 \leq 0.05$) confirm robust thermal–seismic correlations, particularly in tectonically active regions such as SCA and SWS, which exhibit high reliability (FDR < 18.5%) and broad coverage (STCW > 3.7%). In contrast, relatively weak associations in stable zones (e.g., CNA and ECA) highlight the inherent spatial heterogeneity of these responses. Overall, these findings advances the understanding of the spatiotemporal characteristics and clustering phenomena of seismic-related thermal anomalies, providing new insights into the mechanisms underlying seismogenic processes and geodynamic perturbations.

Supplementary Materials: The following supporting information can be downloaded at: https://www.mdpi.com/article/10.3390/rs18020290/s1, File S1: Logical proof of methodology [87]; File S2: Model Across Evaluation Metrics [88]; File S3: Supplementary information on statistics, characteristics, mechanisms, algorithm diagrams, etc.; File S4: model1\model2\model3 Figure.

Author Contributions: P.Y. contributed to writing the original draft, visualization, methodology, investigation, and validation. G.L. contributed to resources and investigation. C.X. was responsible for project administration, resources, investigation, and supervision. L.Z. contributed to methodology, writing—review and editing, funding acquisition, and visualization. Y.X. contributed to resources, writing—review and editing, and funding acquisition. J.Y. contributed to investigation. All authors have read and agreed to the published version of the manuscript.

Funding: This work was funded by the Natural Science Foundation of Xiamen, China (No. 3502Z202472026), and the National Natural Science Foundation of China (No. 42401422).

Data Availability Statement: Global Earthquake Catalog Available from the U.S. Geological Survey (USGS): https://doi.org/10.5066/F7MS3QZH; Global Daily Near-Surface Temperature Data (1 km resolution) Hosted by Iowa State University: https://iastate.figshare.com/authors/Tao_Zhang/9089600 (accessed on 16 December 2024); Blended Sea Surface Temperature Analysis (5 km resolution, Level 4) Provided by NOAA CoastWatch: https://coastwatch.noaa.gov/cwn/index.html (accessed on 1 December 2024); Global Vector Data (Free) Made with Natural Earth: https://www.naturalearthdata.com/downloads/ (accessed on 7 January 2025); IPCC AR6-WGI can be accessed via the GitHub repository: https://github.com/SantanderMetGroup/ATLAS (These release corresponds to v2.0-final release of the Repository supporting the implementation of FAIR principles in the IPCC-WGI Atlas) (accessed on 7 January 2025).

Acknowledgments: We would like to thank the editors and reviewers for their hard work, whose rigorous scientific attitude has greatly improved the quality of this article.

Conflicts of Interest: The authors declare no conflicts of interest.

Abbreviations

The following abbreviations are used in this manuscript:

AEP	Anomaly Emphasis Proximity
FDR	False Discovery Rate
FNR	False Negative Rate
STCW	Spatiotemporal Coverage Width
SU	Spatiotemporal Uncertainty
TSUR	Temporal-Spatial Uncertainty Ratio
SCC	Spatiotemporal Correlation Coefficient
R^2	R-squared
LST	Land Surface Temperature
SST	Sea Surface Temperature
RST	Robust Satellite Techniques

IPCC	Intergovernmental Panel on Climate Change
N and P	Negative and Positive anomalies
TIB	Tibetan-Plateau
SWS	S.W.South-America
SCA	S.Central-America
RFE	Russian-Far-East
CNA	C.North-America
ECA	E.C.Asia
SEA	S.E.Asia
EPO	Equatorial. Pacific-Ocean

References

1. Zhang, Y.; Guo, X.; Shen, W. Thermal infrared anomalies before major earthquakes. *Recent Dev. World Seismol.* **2008**, *11*, 54.
2. Abdrakhmatov, K.; Arrowsmith, R.; Elliott, J.; Grutzner, C.; Mukambayev, A.; Rizza, M.; Shnizai, Z.; Walker, R.; Weldon, R.; Wilkinson, R. Urgent Need for Greater Earthquake Resilience in Continental Asia. *Nat. Geosci.* **2024**, *17*, 818–819. [CrossRef]
3. Albarello, D.; Meletti, C. Earthquake Forecasting and Hazard Assessment: A Preface. *Boll. Geofis. Teor. Appl.* **2012**, *53*, 1–5. [CrossRef]
4. Barkat, A.; Ali, A.; Rehman, K.; Awais, M.; Riaz, M.S.; Iqbal, T. Thermal IR Satellite Data Application for Earthquake Research in Pakistan. *J. Geodyn.* **2018**, *116*, 13–22. [CrossRef]
5. Conti, L.; Picozza, P.; Sotgiu, A. A Critical Review of Ground Based Observations of Earthquake Precursors. *Front. Earth Sci.* **2021**, *9*, 676766. [CrossRef]
6. Qin, K.; Wu, L.X.; Santis, A.D.; Cianchini, G. Preliminary Analysis of Surface Temperature Anomalies That Preceded the Two Major Emilia 2012 Earthquakes (Italy). *Ann. Geophys.* **2012**, *55*, 823–828. [CrossRef]
7. Wang, Y.; Hu, S.; Nie, D.; Zhang, K.; Jiang, G.; Wang, Z. Is the tan-lu fault zone a thermal anomaly belt: Constraints from heat flow in its southern section. *Chin. J. Geophys.* **2019**, *62*, 3078–3094.
8. Bhardwaj, A.; Singh, S.; Sam, L.; Joshi, P.K.; Bhardwaj, A.; Martín-Torres, F.J.; Kumar, R. A Review on Remotely Sensed Land Surface Temperature Anomaly as an Earthquake Precursor. *Int. J. Appl. Earth Obs. Geoinf.* **2017**, *63*, 158–166. [CrossRef]
9. Freund, F. Earthquake Forewarning—A Multidisciplinary Challenge from the Ground up to Space. *Acta Geophys.* **2013**, *61*, 775–807. [CrossRef]
10. Freund, F.; Ouillon, G.; Scoville, J.; Sornette, D. Earthquake Precursors in the Light of Peroxy Defects Theory: Critical Review of Systematic Observations. *Eur. Phys. J. Spec. Top.* **2021**, *230*, 7–46. [CrossRef]
11. Ouzounov, D.; Liu, J.-Y.; Taylor, P.T.; Hattori, K. Editorial: Geospace Observation of Natural Hazards. *Front. Earth Sci.* **2022**, *10*, 836629. [CrossRef]
12. Weiyu, M.; Xuedong, Z.; Liu, J.; Yao, Q.; Zhou, B.; Yue, C.; Kang, C.; Lu, X. Influences of Multiple Layers of Air Temperature Differences on Tidal Forces and Tectonic Stress before, during and after the Jiujiang Earthquake. *Remote Sens. Environ.* **2018**, *210*, 159–165. [CrossRef]
13. Jiao, Z.-H.; Zhao, J.; Shan, X. Pre-Seismic Anomalies from Optical Satellite Observations: A Review. *Nat. Hazards Earth Syst. Sci.* **2018**, *18*, 1013–1036. [CrossRef]
14. Pavlidou, E.; Van der Meijde, M.; Van der Werff, H.; Hecker, C. Time Series Analysis of Land Surface Temperatures in 20 Earthquake Cases Worldwide. *Remote Sens.* **2019**, *11*, 61. [CrossRef]
15. Zhang, Y.; Meng, Q.; Wang, Z.; Lu, X.; Hu, D. Temperature Variations in Multiple Air Layers before the Mw 6.2 2014 Ludian Earthquake, Yunnan, China. *Remote Sens.* **2021**, *13*, 884. [CrossRef]
16. Guo, X.; Zhang, Y.; Wei, C.; Zhong, M.; Zhang, X. Medium wave infrared brightness anomalies of Wenchuan 8.0 and zhongba 6.8 earthquakes. *Acta Seismol. Sin.* **2014**, *35*, 338–344.
17. Yao, Q.; Qiang, Z.; Wang, Y. Co releasefrom thetibetan plateau before earthquakes and increasing temperature anomaly showing in thermalinfrared images of satellite. *Adv. Earth Sci.* **2005**, *20*, 505–510.
18. Guo, X.; Zhang, Y.; Wei, C.; Zhong, M.; Zhang, X. OLR anomalies for the lushan MS7.0 earthquake. *Acta Seismol. Sin.* **2013**, *35*, 731–737+2.
19. Zhang, L.; Wang, P.; Zhang, P.; Sun, X. Thermal infrared anomalies before milin MS6.9 earthquake in 2017. *China Earthq. Eng. J.* **2020**, *42*, 360–367.
20. Zhong, M.; Zhang, Y.; Zhang, X. Thermal infrared anomalies prior to the MS $\geq$ 5 earthquakes in the qilianshan seismic zone. *China Earthq. Eng. J.* **2015**, *37*, 1073–1076.
21. Shao, N.; Meng, Q.; Wei, M.; Lu, X. Analysis of temporal and spatial variation characteristics of seismic brightness temperature anomalies based on background fields before Ms7. 3 yutian earthquake on 2014. *Sci. Technol. Eng.* **2016**, *16*, 136–141.

22. Zhang, X.; Zhang, Y.; Guo, X.; Wei, C.; Zhang, L. Analysis of thermal infrared anomaly in the Nepal MS8.1 earthquake. *Earth Sci. Front.* **2017**, *24*, 227–233. [CrossRef]
23. Freund, F.T. Pre-Earthquake Signals—Part I: Deviatoric Stresses Turn Rocks into a Source of Electric Currents. *Nat. Hazards Earth Syst. Sci.* **2007**, *7*, 535–541. [CrossRef]
24. Freund, F.T. Pre-Earthquake Signals—Part II: Flow of Battery Currents in the Crust. *Nat. Hazards Earth Syst. Sci.* **2007**, *7*, 543–548. [CrossRef]
25. Zhang, Y.; Guo, X.; Wei, C.; Shen, W.; Hui, S. The characteristics of seismic thermal radiation of Japan Ms9.0 and Myanmar Ms7.2 earthquake. *Chin. J. Geophys.* **2011**, *54*, 2575–2580. [CrossRef]
26. Kang, C.; Liu, D.; Jing, F.; Xiong, P.; Cao, Z. Study on the indication of infrared radiation prior to impending strong earthquakes. *Prog. Geophys.* **2011**, *26*, 1897–1905.
27. Wei, C.; Zhang, Y.; Guo, X.; Qin, M.; Ning, Y.; Gao, J. Thermal infrared and long-wave radiation anomalies of yushu MS7.1 earthquake. *Prog. Geophys.* **2013**, *28*, 2444–2452.
28. Pan, Y.; Zhang, X.; Zhang, Y. Analysis of thermal-infrared abnormity on Burma MS6.9 earthquake. *J. Geod. Geodyn.* **2017**, *37*, 1092–1095. [CrossRef]
29. Zhang, A.; Ismaili, S. Thermal infrared anomalies prior to the Shaya M6.1 and Tajikistan M7.2 earthquakes in 2023. *China Earthq. Eng. J.* **2025**, *47*, 199–206+228. [CrossRef]
30. Qiang, Z.; Lin, C.; Li, L.; Xu, M.; Ge, F.; Liu, T.; Zhao, Y.; Guo, M. Satellite thermal infrared image brightness temperature anomalies: Short-term precursors before earthquakes. *Sci. China* **1998**, *6*, 564–574.
31. Guo, X.; Zou, R.; Zhang, X.; Wang, Y. Anomalies in outgoing long-wave radiation for several strong earthquakes in mainland China. *China Earthq. Eng. J.* **2019**, *41*, 1221–1227+1250.
32. Zhong, M.; Zhang, Y.; Guo, X.; Zhang, X. Application of satellite thermal infrared and microwave remote sensing data to earthquake prediction. *China Earthq. Eng. J.* **2014**, *36*, 1059–1063.
33. Bhardwaj, A.; Singh, S.; Sam, L.; Bhardwaj, A.; Martín-Torres, F.J.; Singh, A.; Kumar, R. MODIS-Based Estimates of Strong Snow Surface Temperature Anomaly Related to High Altitude Earthquakes of 2015. *Remote Sens. Environ.* **2017**, *188*, 1–8. [CrossRef]
34. Yang, X.; Lin, W.; Ye, E.; Xu, H.; Xu, Z. Analysis on the mechanisms of coseismic temperature negative anomaly infault zones. *Chin. J. Geophys.* **2020**, *63*, 1422–1430.
35. Ouzounov, D.; Freund, F. Mid-Infrared Emission Prior to Strong Earthquakes Analyzed by Remote Sensing Data. *Adv. Space Res.* **2004**, *33*, 268–273. [CrossRef]
36. Zhang, L.; Jiang, M.; Jing, F. Sea Temperature Variation Associated with the 2021 Haiti Mw 7.2 Earthquake and Possible Mechanism. *Geomat. Nat. Hazards Risk* **2022**, *13*, 2840–2863. [CrossRef]
37. Fulton, P.M.; Brodsky, E.E.; Kano, Y.; Mori, J.; Chester, F.; Ishikawa, T.; Harris, R.N.; Lin, W.; Eguchi, N.; Toczko, S.; et al. Low Coseismic Friction on the Tohoku-Oki Fault Determined from Temperature Measurements. *Science* **2013**, *342*, 1214–1217. [CrossRef]
38. Blackett, M.; Wooster, M.J.; Malamud, B.D. Exploring Land Surface Temperature Earthquake Precursors: A Focus on the Gujarat (India) Earthquake of 2001. *Geophys. Res. Lett.* **2011**, *38*, L15303. [CrossRef]
39. Jiao, Z.-H.; Shan, X. Statistical Framework for the Evaluation of Earthquake Forecasting: A Case Study Based on Satellite Surface Temperature Anomalies. *J. Asian Earth Sci.* **2021**, *211*, 104710. [CrossRef]
40. Wu, W.; Shan, X.; Qu, C.; Li, X. Comparative study on thermal anomalies detection method before strong earthquake: Taking the 2014 MW6.9 yutian earthquake as an example. *Seismol. Geol.* **2022**, *44*, 1503–1520.
41. Tramutoli, V.; Di Bello, G.; Pergola, N.; Piscitelli, S. Robust Satellite Techniques for Remote Sensing of Seismically Active Areas. *Ann. Geofis.* **2001**, *44*, 295–312. [CrossRef]
42. Tramutoli, V. Robust Satellite Techniques (RST) for Natural and Environmental Hazards Monitoring and Mitigation: Theory and Applications. In Proceedings of the 2007 International Workshop on the Analysis of Multi-temporal Remote Sensing Images, Louvain, Belgium, 18–20 July 2007; pp. 139–144.
43. Aliano, C.; Corrado, R.; Filizzola, C.; Genzano, N.; Pergola, N.; Tramutoli, V. Robust TIR Satellite Techniques for Monitoring Earthquake Active Regions: Limits, Main Achievements and Perspectives. *Ann. Geophys.* **2008**, *51*, 303–317. [CrossRef]
44. Jiao, Z.; Shan, X. Pre-Seismic Temporal Integrated Anomalies from Multiparametric Remote Sensing Data. *Remote Sens.* **2022**, *14*, 2343. [CrossRef]
45. Akhoondzadeh, M. A Comparison of Classical and Intelligent Methods to Detect Potential Thermal Anomalies before the 11 August 2012 Varzeghan, Iran, Earthquake (m_w = 6.4). *Nat. Hazards Earth Syst. Sci.* **2013**, *13*, 1077–1083. [CrossRef]
46. Xiong, P.; Shen, X.H.; Bi, Y.X.; Kang, C.L.; Chen, L.Z.; Jing, F.; Chen, Y. Study of Outgoing Longwave Radiation Anomalies Associated with Haiti Earthquake. *Nat. Hazards Earth Syst. Sci.* **2010**, *10*, 2169–2178. [CrossRef]
47. Li, Q.; Zhang, Y.; Lv, J.; Ren, J.; Zhang, L.; Zhang, X. Thermal infrared anomaly occurring before the Jinggu, Yunnan MS6.6 earthquake on October 7, 2014. *China Earthq. Eng. J.* **2015**, *37*, 1007–1012.

48. Zhan, X.; Lin, X.; Kong, X.; Xiong, P.; Chen, L.; Zheng, Z. Application of cusum in noaa satellite data anomaly analysis before earthquake. *Comput. Appl. Softw.* **2015**, *32*, 232–235.
49. Jing, F.; Shen, X.; Wang, H.; Kang, C.; Xiong, P. Infrared characteristics analysis of the 2015 Nepal MS8.1 earthquake. *Acta Seismol. Sin.* **2016**, *38*, 429–437.
50. Liu, W.; Meng, Q.; Zhang, J.; Zhang, Y.; Lu, X.; Meng, Y. Seismic thermal infrared anomaly extraction based on skewness. *Seismol. Geol.* **2020**, *42*, 1509–1524.
51. Song, D.; Zhang, M.; Shan, X.; Cui, J.; Wang, B. Construction method of seismothermal infrared background field based on GPR-LSTM. *Seismol. Geol.* **2024**, *46*, 492–511.
52. Gornyi, V.; Salman, A.; Tronin, A.; Shilin, B. The outgoing infrared radiation of the earth as an indicator of seismic activity. *Dokl. Akad. Nauk. SSSR* **1988**, *301*, 67–69.
53. Lin, C.; Wang, X.; Qiang, Z. Satellite thermal infrared anomaly warming and precursors before the earthquake in Changshu. *Chin. Sci. Bull.* **1992**, *9*, 821–824.
54. Ouzounov, D.; Liu, D.; Chunli, K.; Cervone, G.; Kafatos, M.; Taylor, P. Outgoing Long Wave Radiation Variability from IR Satellite Data Prior to Major Earthquakes. *Tectonophysics* **2007**, *431*, 211–220. [CrossRef]
55. Tronin, A.A.; Hayakawa, M.; Molchanov, O.A. Thermal IR Satellite Data Application for Earthquake Research in Japan and China. *J. Geodyn.* **2002**, *33*, 519–534. [CrossRef]
56. Mignan, A.; Ouillon, G.; Sornette, D.; Freund, F. Global Earthquake Forecasting System (GEFS): The Challenges Ahead. *Eur. Phys. J. Spec. Top.* **2021**, *230*, 473–490. [CrossRef]
57. Picozza, P.; Conti, L.; Sotgiu, A. Looking for Earthquake Precursors from Space: A Critical Review. *Front. Earth Sci.* **2021**, *9*, 676775. [CrossRef]
58. Meng, Y.; Meng, Q.; Zhou, S.; Zhang, Y. Extraction and analysis of seismic thermal anomalies in Xinjiang based on robust satellite techniques. *Acta Seismol. Sin.* **2020**, *42*, 205–215+245.
59. Zhang, Y.; Liu, Q.; Guo, X. Progress in application and study of the technology of satellite infrared remote sensing on earthquake prediction. *Northwest Seismol. J.* **2004**, *26*, 357–361.
60. Zhang, Y.; Meng, Q.; Ouillon, G.; Zhang, L.; Hu, D.; Ma, W.; Sornette, D. Long-Term Statistical Evidence Proving the Correspondence between Tir Anomalies and Earthquakes Is Still Absent. *Eur. Phys. J. Spec. Top.* **2021**, *230*, 133–150. [CrossRef]
61. Freund, F. Pre-Earthquake Signals: Underlying Physical Processes. *J. Asian Earth Sci.* **2011**, *41*, 383–400. [CrossRef]
62. Yang, X.; Lin, W.; Tadai, O.; Zeng, X.; Yu, C.; Yeh, E.-C.; Li, H.; Wang, H. Experimental and Numerical Investigation of the Temperature Response to Stress Changes of Rocks. *J. Geophys. Res. Solid Earth* **2017**, *122*, 5101–5117. [CrossRef]
63. Chen, S.; Liu, P.; Feng, T.; Wang, D.; Jiao, Z.; Chen, L.; Xu, Z.; Zhang, G. Exploring Changes in Land Surface Temperature Possibly Associated with Earthquake: Case of the April 2015 Nepal Mw 7.9 Earthquake. *Entropy* **2020**, *22*, 377. [CrossRef] [PubMed]
64. Ahmad, N.; Barkat, A.; Ali, A.; Sultan, M.; Rasul, K.; Iqbal, Z.; Iqbal, T. Investigation of Spatio-Temporal Satellite Thermal IR Anomalies Associated with the Awaran Earthquake (Sep 24, 2013; M 7.7), Pakistan. *Pure Appl. Geophys.* **2019**, *176*, 3533–3544. [CrossRef]
65. Genzano, N.; Filizzola, C.; Hattori, K.; Pergola, N.; Tramutoli, V. Statistical Correlation Analysis between Thermal Infrared Anomalies Observed from MTSATs and Large Earthquakes Occurred in Japan (2005-2015). *J. Geophys. Res.-Solid Earth* **2021**, *126*, e2020JB020108. [CrossRef]
66. Filizzola, C.; Corrado, A.; Genzano, N.; Lisi, M.; Pergola, N.; Colonna, R.; Tramutoli, V. RST Analysis of Anomalous TIR Sequences in Relation with Earthquakes Occurred in Turkey in the Period 2004–2015. *Remote Sens.* **2022**, *14*, 381. [CrossRef]
67. Yao, Q.; Qiang, Z.; Li, M. Thermal infrared anomalies as a precursor of strong earthquakes in the distant future. *Transl. World Seismol.* **2020**, *51*, 224–235. [CrossRef]
68. Qiang, Z.; Ma, A.; Zeng, Z.; Wang, J. A study of the method of satellite thermal infrared earthquake prediction in imminence. *Earth Sci. Front.* **2010**, *17*, 254–262.
69. Cicerone, R.D.; Ebel, J.E.; Britton, J. A Systematic Compilation of Earthquake Precursors. *Tectonophysics* **2009**, *476*, 371–396. [CrossRef]
70. Bonan, G.B. Forests and Climate Change: Forcings, Feedbacks, and the Climate Benefits of Forests. *Science* **2008**, *320*, 1444–1449. [CrossRef]
71. Cattiaux, J.; Ribes, A.; Thompson, V. Searching for the Most Extreme Temperature Events in Recent History. *Bull. Am. Meteorol. Soc.* **2024**, *105*, E239–E256. [CrossRef]
72. Magnan, A.K.; Pörtner, H.-O.; Duvat, V.K.E.; Garschagen, M.; Guinder, V.A.; Zommers, Z.; Hoegh-Guldberg, O.; Gattuso, J.-P. Estimating the Global Risk of Anthropogenic Climate Change. *Nat. Clim. Change* **2021**, *11*, 879–885. [CrossRef]
73. Shi, J.-R.; Santer, B.D.; Kwon, Y.-O.; Wijffels, S.E. The Emerging Human Influence on the Seasonal Cycle of Sea Surface Temperature. *Nat. Clim. Change* **2024**, *14*, 364–372. [CrossRef]
74. Zhang, Y.; Meng, Q.; Ouillon, G.; Sornette, D.; Ma, W.; Zhang, L.; Zhao, J.; Qi, Y.; Geng, F. Spatially Variable Model for Extracting TIR Anomalies before Earthquakes: Application to Chinese Mainland. *Remote Sens. Environ.* **2021**, *267*, 112720. [CrossRef]

75. Eyring, V.; Bony, S.; Meehl, G.A.; Senior, C.A.; Stevens, B.; Stouffer, R.J.; Taylor, K.E. Overview of the Coupled Model Intercomparison Project Phase 6 (CMIP6) Experimental Design and Organization. *Geosci. Model Dev.* **2016**, *9*, 1937–1958. [CrossRef]
76. Iturbide, M.; Gutiérrez, J.M.; Alves, L.M.; Bedia, J.; Cerezo-Mota, R.; Cimadevilla, E.; Cofiño, A.S.; Di Luca, A.; Faria, S.H.; Gorodetskaya, I.V.; et al. An Update of IPCC Climate Reference Regions for Subcontinental Analysis of Climate Model Data: Definition and Aggregated Datasets. *Earth Syst. Sci. Data* **2020**, *12*, 2959–2970. [CrossRef]
77. Mansouri Daneshvar, M.R.; Freund, F.T.; Ebrahimi, M. Spatial and Temporal Analysis of Climatic Precursors before Major Earthquakes in Iran (2011–2021). *Sustainability* **2023**, *15*, 11023. [CrossRef]
78. Zhang, T.; Zhou, Y.; Zhao, K.; Zhu, Z.; Chen, G.; Hu, J.; Wang, L. A Global Dataset of Daily Maximum and Minimum Near-Surface Air Temperature at 1 Km Resolution over Land (2003–2020). *Earth Syst. Sci. Data* **2022**, *14*, 5637–5649. [CrossRef]
79. Harris, A.; Mittaz, J.; Sapper, J.; Wick, G.; Zhu, X.; Dash, P.; Koner, P. A New High-Resolution Sea Surface Temperature Blended Analysis. *Bull. Am. Meteorol. Soc.* **2017**, *98*, 1015–1026. [CrossRef]
80. Song, D.; Zang, L.; Shan, X.; Yuan, Y.; Cui, J.; Shao, H.; Shen, C.; Shi, H. A study on the algorithm for extracting earthquake thermal infrared anomalies based on the yearly trend of lst. *Seismol. Geol.* **2016**, *38*, 680–695.
81. Meng, Q.; Lu, X.; Li, X.; Shen, X.; Geng, F.; Wang, Y. Research progress in earthquake infrared background field and brightness temperature background field foundation of the demonstration areas. *Acta Seismol. Sin.* **2016**, *38*, 438–447+508.
82. Ying, Z.; Sornette, D.; Meng, Q. A New 3-D Error Diagram for a More Balanced Assessment of Binary Alarms for Predicting Earthquakes: Application to TIR Anomalies in Sichuan Area, China. *IEEE Trans. Geosci. Remote Sens.* **2023**, *61*, 5003311. [CrossRef]
83. Lockner, D.; Okubo, P. Measurements of Frictional Heating in Granite. *J. Geophys. Res.* **1983**, *88*, 4313–4320. [CrossRef]
84. de Lorenzo, S.; Loddo, M. Effect of Frictional Heating and Thermal Advection on Pre-Seismic Sliding: A Numerical Simulation Using a Rate-, State- and Temperature-Dependent Friction Law. *J. Geodyn.* **2010**, *49*, 1–13. [CrossRef]
85. Wu, L.; Qin, K.; Liu, S.; De Santis, A.; Cianchini, G. Importance of Lithosphere-Coversphere-Atmosphere Coupling to Earthquake Anomaly Recognition. In Proceedings of the 2012 IEEE International Geoscience and Remote Sensing Symposium, Munich, Germany, 22–27 July 2012; pp. 3532–3535.
86. Xo, X.; Chen, S.; Zhang, S.; Dai, R. Analysis of Potential Precursory Pattern at Earth Surface and the Above Atmosphere and Ionosphere Preceding Two Mw $\geq$ 7 Earthquakes in Mexico in 2020–2021. *Earth Space Sci.* **2022**, *9*, e2022EA002267. [CrossRef]
87. Liu, P.; Liu, L.; Chen, S.; Chen, G.; Ma, J. Heat penetrability index (hpi) method for distilling subsurface thermal information from satellite infrared images. *Seismol. Geol.* **2004**, *26*, 519–527.
88. Zhang, T.; Yang, X.; Lu, Q.; Long, F. The characteristics of satellite thermal infrared background field in the eastern qinghai-tibet plateau and surrounding areas. *Sci. Technol. Eng.* **2021**, *21*, 9217–9223.

Disclaimer/Publisher's Note: The statements, opinions and data contained in all publications are solely those of the individual author(s) and contributor(s) and not of MDPI and/or the editor(s). MDPI and/or the editor(s) disclaim responsibility for any injury to people or property resulting from any ideas, methods, instructions or products referred to in the content.